

האוניברסיטה העברית בירושלים
הפקולטה למתמטיקה ולמדעי הטבע - מכון רקח לפיסיקה

על מקור התנע הזוויתי בגלקסיות
On the Origin of Angular Momentum in Galaxies

by

Mark Danovich 303898266

under the supervision of

Prof. Avishai Dekel

Thesis Submitted for the Degree of
Master of Science

December 2013

טבת התשע"ד

תקציר

התנע הזוויתי של גלקסיות דיסקה הוא גודל בעל חשיבות רבה להבנת תהליך ההיווצרות והתכונות של עצמים אלו, שכן אלו מערכות הנתמכות ע"י סיבובן. מקור התנע הזוויתי בגלקסיות הוא בעיה רב שלבית הנפרשת על מספר סקלות החל מהמארג הקוסמי המתאר את התפלגות החומר ביקום בסקלות הגדולות ביותר (מיליוני פרסק) דרך ההילות האפלות בהן הגלקסיות שוכנות (מאות אלפי פרסק) ועד דיסקת הגלקסיה עצמה (אחדות עד עשרות פרסק). בעבודה זאת אנו חוקרים את המקור והתכונות של התנע הזוויתי בגלקסיות דיסקה בזמנים מוקדמים באמצעות סימולציות הידרו-קוסמולוגיות של 30 גלקסיות. אנו מציעים ובוחנים את התמונה הבאה: התנע הזוויתי של הדיסקה מקורו בדרך כלל ב-3 זרמים הנטיים להיות במישור עם מרכז הגלקסיה, אשר מתארים את הזרמים של המארג הקוסמי ועוברים דרך 4 שלבים ב-4 איזורים. בשלב 1, אשר מתרחש בסקלה של המארג הקוסמי, הבריונים והחומר האפל רוכשים תנע זוויתי דומה דרך מומנטים המופעלים מהסביבה. התנע הזוויתי של הזרמים הקרים בא לידי ביטוי ע"י פרמטר פגיעה בטווח $(0-0.3)R_v$, עם פרמטר ספין כולל של ~ 0.1 . בשלב 2, התנע הזוויתי של הרכיבים השונים נישא לעבר ההילה. הדומיננטיות של הזרמים הקרים מוגברת בשלב זה בעקבות להתפלגות המרחבית של הזרמים, המובילה לקוהרנטיות גדולה יותר בחיבור התנע הזוויתי ופחות ערבוב בתוך ההילה. החומר האפל עובר ויריאליזציה בתוך ההילה, מתערבב עם חומר בעל תנע זוויתי נמוך יותר, המוביל לפרמטר ספין כולל של ~ 0.04 . בשלב 3, באיזור פרמטר הפגיעה, הזרמים הקרים נעצרים ע"י התנע הזוויתי שלהם, מאבדים חלק ממהירותם, ונכנסים למסלול מסביב לדיסקה במרכז. בכך הם יוצרים מבנה דיסקתי חיצוני המגיע עד $0.3R_v \sim$ ומוטה ביחס לדסקה הפנימית. באיזור זה הגז הקר חווה מומנטים גרביטציוניים משמעותיים, הגורמים לגז לאבד תנע זוויתי עד לפרמטר ספין של ~ 0.04 , ולהתחבר עם מישור הדיסקה הפנימית. בשלב 4, המתרחש בתוך הדיסקה הפנימית, היזון חוזק מהכוכבים גורם להעפת חומר עם תנע זוויתי נמוך, ואי יציביות בתוך הדיסק גורמות למומנטים המובילים תנע זוויתי החוצה וגז לעבר המרכז.

Acknowledgments

I would like to thank my advisor Prof. Avishai Dekel and the cosmology group members (especially to Dr. Dylan Tweed, Dr. Daniel Ceverino and Nir Mandelker) for helpful discussions, ideas and general support. I would like to thank Dr. Oliver Hahn for a fruitful collaboration and discussions. Finally, I would like to give special thanks to my parents for their support during my studies.

Abstract

The angular momentum (AM) of disc galaxies is of major importance for the understanding of how these systems form and their properties, as these are rotationally supported systems. The origin of the AM in galaxies is a multi-stage and multi-scale problem which starts from the cosmic web scale (Mpc) through the dark matter (DM) halo (100kpc) down to the disc itself (10kpc). In this work we study the origin and properties of AM in high- z disc galaxies using zoom-in AMR hydro-cosmological simulations of 30 massive galaxies with $M_v \sim 10^{12} M_\odot$ at the redshift range $z = 4 - 1.5$. We propose and test the following picture: the disc AM originates from typically 3 co-planar streams of cold gas that trace the filaments of the cosmic web and go through 4 stages of evolution in 4 zones. In stage I, taking place on the cosmic web scale, the baryons and DM gain AM through linear tidal torques from the cosmic web. The streams AM is expressed as an impact parameter in the range $(0 - 0.3)R_v$, with a total spin of $\lambda \sim 0.1$. In stage II, the AM of the different components is transported into the halo. The dominance of the cold gas spin is enhanced in this stage due to its spatial distribution in filaments, leading to higher coherence in the AM addition and less mixing within the halo. The DM virializes within the halo, mixing with older material with lower AM resulting in a lower total spin of $\lambda \sim 0.04$. In stage III, near the pericenter, the streams dissipate and enter into an orbit around the center, forming an extended outer disc and tilted relative to the inner disc out to $\sim 0.3R_v$. In this region, torques exerted on the cold gas, make it lose AM to ~ 0.04 , spiral in and settle into the disc inner plane. In stage IV, taking place within the disc, outflows remove low-spin gas and torques associated with violent disc instability drive the gas into a central bulge.

Contents

1	Introduction	1
1.1	AM in DM halos and galaxies	1
1.2	The cosmic web	2
1.3	Cold streams	3
1.4	Tidal Torque Theory	4
1.5	ART simulation	5
2	Co-planar streams and pancakes	8
2.1	Cold streams identification	8
2.2	Streams co-planarity	10
2.3	Mass and AM distribution in streams	12
2.4	Stream plane extension, alignment and stability	14
3	AM content and transport in DM halos	18
3.1	The spin parameter	18
3.2	Kinematics and coherence	25
3.3	Disc and halo AM alignments	34
3.4	Disc spin parameter and radius	35
4	Torques and AM exchange in the inner halo	41
4.1	The 'Messy Region'	41
4.2	Torques and AM exchange	45
5	Summary and discussion	50
5.1	Summary	50
5.2	Open questions and caveats	54
5.3	Suggested observations and future work	55

Chapter 1

Introduction

1.1 AM in DM halos and galaxies

The origin of AM in dark matter halos and galaxies is a fundamental problem in the field of galaxy formation within the standard model of cosmology called Λ CDM. Its fundamental importance lies in that disc galaxies are rotationally supported systems in which the AM they possess defines main features such as their size, surface density and rotational velocity which are all observationally available parameters to test the understanding of galaxy formation. The first major advance was due to the works by (Peebles, 1969; Doroshkevich, 1970; White, 1984) which argued that density perturbations growing from the primordial density fluctuations field, acquire AM through tidal interactions with neighboring density perturbations, until the perturbation decouples from the expanding background and collapses to form a virialized halo. (Fall and Efstathiou, 1980) extended this picture to include the baryonic component and explained the formation of a flat rotating disc by incorporating the tidal torque theory with the cooling and collapse of the shock heated gas to the halo center. They assumed that the gas obtains similar specific AM as the DM and it conserves its specific AM during the collapse to form a the rotationally supported disc. Recent advances, both analytic and numerical, have changed the picture of how gas is accreted into dark matter halos. Analytic works by (Birnboim and Dekel, 2003) and numerical simulations (Dekel et al., 2009) have shown that in some cases relevant in the relatively high redshift universe, gas can cool efficiently and does not shock heat at the virial radius as was the standard picture due to (Rees and Ostriker, 1977), but flows as cold dense gas into the halo, along dark matter filaments. The filaments are the dominant feature of the large scale structure in the universe both visually and in terms of mass as was shown qualitatively in galaxy surveys and in numerical simulations. This large scale distribution is known as the cosmic web - a complex network of filaments, sheets, nodes and voids first envisioned by Zel'dovich (Zeldovich, 1970). The anisotropic nature and dominance of the filaments in the build up of dark matter halos and the baryons within them, can have important implications on AM related questions. In this work, we study the implications of these new features as seen in hydro-cosmological simulations, on the

AM origin and properties in DM halos and galaxies.

1.2 The cosmic web

According to the Λ CDM model, the large scale structure in the universe originated from primordial quantum fluctuations which grew and became density fluctuations in the matter distribution following inflation. These density fluctuations grew through gravitational instability and collapsed to form dark matter halos and the present day structure in the universe. The process of gravitational collapse is complicated and non-linear, however the resulting distribution of matter is found to be ordered in a form of a web called the cosmic web, consisting of 4 main features: filaments, sheets, nodes and voids. The idea of a cosmic web gained support both from observations in the form of galaxy surveys (Hucra et al., 1983; Colless, 1999; Adelman-McCarthy, 2008) as well as from N-body and full hydrodynamical cosmological simulations (Klypin and Shandarin, 1983; Springel et al., 1996; Klypin et al., 2011). The first theoretical idea of the cosmic web resulting from gravitational instability was due to Zel'dovich (Zeldovich, 1970) and later extended by (Bond et al., 1996). The Zel'dovich approximation for the study of this process is based on a Lagrangian approach to the evolution of the initial density field in the linear regime, defined by $\delta = \frac{\rho - \bar{\rho}}{\bar{\rho}} < 1$, where $\bar{\rho}$ is the mean density in the universe. The approximation consists of a mapping between the initial Lagrangian position q of a fluid element to the Eulerian position at a later time x :

$$\mathbf{x}(q, t) = \mathbf{q} + D(t)\nabla\Phi(q) \quad (1.1)$$

Where $D(t)$ is the linear growth rate of the density fluctuations and $\Phi(q)$ is the initial gravitational potential. The second term is in general termed the displacement field. Considering a region in the Lagrangian frame of volume d^3q , conservation of mass implies: $\rho(x, t)d^3x = \bar{\rho}d^3q$ where $\bar{\rho}$ is the unperturbed density. Performing a change of variables on the lefthand side gives:

$$\rho(q, t)\left|\frac{\partial\mathbf{x}}{\partial\mathbf{q}}\right| = \bar{\rho} \quad (1.2)$$

from which we get using (1.1), the evolution of the density at the initial position of the fluid element:

$$\rho(q, t) = \frac{\bar{\rho}}{\det[\delta_{ij} + D(t)\frac{\partial^2\Phi(q)}{\partial_i\partial_j}]} \quad (1.3)$$

Where δ_{ij} is the unity matrix. The second term in the denominator contains a symmetric matrix of the partial derivatives of the gravitational potential, it therefore has 3 real eigenvalues which we can in general write as $-\lambda_3 \geq -\lambda_2 \geq -\lambda_1$. We can write the density in terms of these eigenvalues:

$$\rho(q, t) = \frac{\bar{\rho}}{(1 - D(t)\lambda_1(q))(1 - D(t)\lambda_2(q))(1 - D(t)\lambda_3(q))} \quad (1.4)$$

From this we get the main result of the Zel'dovich approximation: a sequential collapse of matter along the axes set by the tidal tensor's eigenvalues. To see this, we note that the density diverges once one of the terms in the denominator becomes zero, at which point, particles cross each other's paths and the original mapping becomes singular. Since $D(t)$ is an increasing function with time, the density will diverge first along the axis with the largest positive eigenvalue resulting in a planar structure or a pancake normal to this axis. Following the first crossing the expression diverges and becomes mathematically incorrect, however physically the density doesn't diverge and the particles (dark matter in this case) will pass through each other, therefore one can qualitatively continue the approximation beyond the first divergence. The second collapse will occur along the axis corresponding to the second largest and positive eigenvalue leading to a filamentary structure and finally in the case where all eigenvalues are positive there will be a collapse along all three axes. Therefore, the Zel'dovich approximation naturally explains the origin of the anisotropic structures seen in the cosmic web. The sign and size of the eigenvalues of the local tidal-tensor determine the morphology of the density field in that region according to: $(+,+,+)$ -node, $(+,-,-)$ -pancake, $(+,+,-)$ -filament and $(-,-,-)$ -void, where in the last case the density field expands in all three axes resulting in a void. In the linear regime of the Gaussian random density fluctuation field, (Doroshkevich, 1970) obtained the distribution of the eigenvalues of the deformation/tidal tensors from which one gets the volume and mass fractions of the four morphologies with 42% in filaments and sheets, and 8% in nodes and voids. In the non-linear regime (depending on the smoothing scales) various studies (Hahn et al., 2007; Aragon-Calvo et al., 2010; Shen et al., 2006), using the methods of the eigenvalues and excursion-set models for the collapse of triaxial structures have demonstrated the dominance of the filaments in terms of the mass. This dominance was explained by (Bond et al., 1996), who pointed out the importance of the correlation between neighboring density peaks. Rare density peaks present already in the primordial density field, will result in alignment of the strain field ($e_{ij} = -(\nabla_i s_j + \nabla_j s_i)/2$, where s is the displacement field defined above for the linear theory) along the long axis between the peaks, leading to the formation of a filamentary-like overdensity bridge that will grow and become more dominant in the non-linear regime.

1.3 Cold streams

In the old paradigm of disc galaxy formation, the gas that falls within a virialized dark matter halo to form the galaxy is shock heated near the virial radius and is heated to $T_{shock} \geq 3T_v/8$, where T_v is the virial temperature of the halo. The gas then radiatively cools from inside out, and as long as the cooling time is less than a Hubble time ($t_h \sim H^{-1}$), a disc will form. However, a more careful analysis of the shock stability criteria by (Birnboim and Dekel, 2003), led to a new scenario in which the stability of the shock is determined by two competing processes i.e. the cooling of the post-shock gas and the compression of the gas due to the shock front. If the cooling is efficient enough, the gas will not have enough pressure to support the shock, and it will collapse cold to the center.

Otherwise, if the compression of the gas is efficient enough, then the pressure of the post-shock gas will be able to support the shock. This is summarized by the condition for stability in terms of the time scales for compression $\rho/\dot{\rho}$ and cooling (e/q , where q is the cooling rate depending on the density and the cooling function): $t_{compress} < t_{cool}$. It was found that there exists a critical mass $\sim 10^{11.6}M_{\odot}$ above which the shock is stable against the gravitational collapse due to the pressure of the post shocked gas, and thus the gas falling into the halo is shock-heated and the halo is filled with hot gas that is slowly cooling. This is where the cosmic web enters the picture. At high enough redshifts, massive halos above the critical mass, are high- σ peaks in the distribution of halo masses. As such, these will be found in the intersection of filaments in the hierarchical cosmic web. These filaments at early times are thinner and denser than the mean density within the halo. The gas which follows the distribution of the dark matter, will stream along these filaments. The high density of the gas within the filaments allows it to cool rapidly ($T < 10^5 K$) and avoid shock heating, as the gas outside the filaments experiences. This notion of cold streams within dark matter haloes, can obviously have significant effect on the formation of large rotating disc galaxies in terms of mass, star formation and angular momentum, as was pointed out and studied in (Dekel et al., 2009; Brooks et al., 2009; Tillson et al., 2012). We summarize that massive halos at high-redshifts are found at the nodes of the cosmic web which are at the intersection of dark matter filaments containing cold dense gas which flows into the center of the dark matter halo.

1.4 Tidal Torque Theory

The pioneering works by (Peebles, 1969; Doroshkevich, 1970; White, 1984) have provided an understanding for the origin of AM in DM halos through tidal interactions between the inertia tensor of the Lagrangian region which will collapse to form the halo and the external large scale tidal field set by the region's environment. This interaction results in torques which spin the Lagrangian region giving the dark matter and baryons within the region initial angular momentum, before the region collapses to form the halo. A detailed derivation of this idea goes as follows: the trajectory of a particle in the linear regime can be approximated by the Zel'dovich approximation, in physical coordinates:

$$r_j = a(t)(q_j + D(t)\Phi_{,j}) \quad (1.5)$$

Where we mark derivative with respect to component j with $_{,j}$. The separation of the trajectory of a near by particle is then given by:

$$\delta r_j = \frac{\partial r_j}{\partial r_k} \delta q_k = a \delta q_j + a D \Phi_{,jk} \delta q_k, \quad (1.6)$$

and the velocity of the particle in that trajectory is given by the time derivative:

$$\delta v_j = \frac{d \delta r_j}{dt} = \dot{a} \delta q_j + \frac{d}{dt} (a D) \Phi_{,jk} \delta q_k \quad (1.7)$$

Using these, we get an expression for the angular momentum of a volume element dV with density ρ and a distance δr_j from the original trajectory which can be taken as the CM of some distribution of particles.

$$dL_j = \rho dV \epsilon_{jkl} [(a(t)\delta q_k + a(t)D(t)\Phi_{,km} \delta q_m)(\dot{a}(t)\delta q_l + \frac{d}{dt}(a(t)D(t)\Phi_{,ln} \delta q_n)] \quad (1.8)$$

Using the anti-symmetry of ϵ_{jkl} we are left with one term,

$$dL_j = \rho dV \epsilon_{jkl} a^2(t) \dot{D}(t) \Phi_{,ln} \delta q_n \delta q_k \quad (1.9)$$

Integrating over the region gives:

$$L_j = \epsilon_{jkl} a^2(t) \dot{D}(t) T_{ln} I_{nk} \quad (1.10)$$

Where $T_{ln} = \Phi_{,ln}$ is the tidal tensor and $I_{nk} = \int \rho dV \delta q_n \delta q_k$ is the inertia tensor. We see that a non-zero angular momentum can be acquired only if the inertia tensor and the tidal tensor are misaligned and the protogalaxy is non spherical. Finally the time dependence of the AM is $L \propto a(t)\dot{D}(t)$ which for an EdS universe ($\Omega_m = 1$, a good approximation for redshifts above $z = 1$), gives $L \propto a(t)^{3/2} = t$. The idea of tidal torques as the main source of AM for dark matter halos have led to the development of models for the formation of rotating disc galaxies. In these models (Fall and Efstathiou, 1980; Mo et al., 1998), an important assumption is made regarding the AM of the baryons, namely that both baryons and DM are acted on by the same tidal torques and therefore should have the same initial specific AM. The baryons which were shock heated to the virial temperature during their accretion to the halo, cool radiatively and loose energy causing them to collapse. The second assumption in these models is that this collapse conserves in detail (at every radius) the initial AM, thus connecting the disc AM and the halo's. However these assumptions and the tidal torque theory have their shortcomings as noted in various studies. Tidal torque theory poorly predicts the final AM amplitude and direction of dark matter halos as tested in numerical simulations, mainly due to non linear processes occurring beyond the scope of the linear theory, furthermore, it doesn't account explicitly for the contribution of mergers, however this doesn't imply that the idea behind the model is wrong. The assumptions made by the models connecting the disc to the halo, fail to reproduce the observed surface densities of disc galaxies, if one assumes similar distribution of specific AM for the baryons forming the disc and the DM (Bullock et al., 2001). These remarks demonstrate that the origin, properties and evolution of AM in disc galaxies is still poorly understood.

1.5 ART simulation

The data we analyze in this work consists of zoom-in simulations of galaxies which were simulated using the ART code. The hydro-gravitational code ART (Kravtsov et al., 1997), uses the adaptive mesh refinement (AMR) approach to follow the Eulerian gas dynamics.

The cosmological model adopted in the simulation is the standard Λ CDM cosmology with the WMAP5 cosmological parameters $\Omega_m = 0.27, \Omega_\Lambda = 0.73, \Omega_b = 0.045, h = 0.7$ and $\sigma_8 = 0.82$. The code implements many sub-grid physical processes relevant for galaxy formation, these include: gas cooling by atomic hydrogen and helium, metal and molecular hydrogen cooling, photo-ionization heating by a UV background with partial self shielding, stochastic star formation in cells with gas temperature $T \leq 10^4 K$ and densities $n_H \geq 1 cm^{-3}$ at a rate consistent with the Kennicutt-Schmidt law, stellar mass loss, metal enrichment of the ISM and stellar feedback from winds and supernovae which are implemented by locally injecting the thermal energy to the gas at a constant rate. A number of halos were selected from the N-body simulation and then re-simulated by including the gas and refining a mesh within a zoom-in Lagrangian volume that contains the mass that is found within $2R_v$ at $z = 1$ (a sphere of about 1Mpc) and embedded in a cosmological box of side 20 and $40h^{-1}$ Mpc. The zoom-in regions were simulated with $\sim (4 - 11) \times 10^6$ dark matter particles of mass $6.6 \times 10^5 M_\odot$ each, and star particles of a minimum mass of $10^4 M_\odot$. The AMR cells are refined once the mass in them is higher than $2 \times 10^6 M_\odot$ (3 dark matter particles) or a gas mass higher than $1.5 \times 10^5 M_\odot$. The minimum cell size ranges between $30 - 70 pc$ physical. We use 29 of the re-simulated dark matter halos (see table) each containing a disc galaxy in the center. We analyze the halos in the redshift range $z \approx 4 - 1.5$. The virial masses at $z = 2.5$ are in the range $10^{11.1} M_\odot$ to $10^{12.2} M_\odot$. The center of each galaxy was set to the position of the highest density gas cell. The velocities of the gas, stars and DM were corrected to the rest frame of the galaxy, and all angular momentum calculations were done in this frame with respect to the galaxy center. We summarize the simulated halos details in the following table.

Table 1.1: Details of the halos used from the ART simulation. For each halo we specify its name, virial mass and radius and the final snapshot used in the analysis.

i	Halo	$M_v[10^{12}M_\odot]$	$R_v[kpc]$	a_{final}	i	Halo	$M_v[10^{12}M_\odot]$	$R_v[kpc]$	a_{final}
1	MW1	1.32	141.75	0.4	16	SFG8	1.42	128.0	0.35
2	MW2	0.946	108.75	0.34	17	SFG9	3.54	197.75	0.4
3	MW3	1.28	140.25	0.4	18	VL01	1.89	148.75	0.37
4	MW4	1.91	153.75	0.38	19	VL02	0.929	126.0	0.4
5	MW5	3.51	155.5	0.4	20	VL03	1.09	107.0	0.32
6	MW6	0.781	118.75	0.4	21	VL04	1.20	137.0	0.4
7	MW7	0.494	102.0	0.4	22	VL05	2.08	165.25	0.4
8	MW8	0.290	85.5	0.4	23	VL06	0.824	121.5	0.4
9	MW9	0.344	90.5	0.4	24	VL07	1.68	128.5	0.33
10	MW10	1.41	145.0	0.4	25	VL08	1.13	135.0	0.34
11	MW11	0.611	109.75	0.4	26	VL09	0.543	91.25	0.34
12	MW12	3.49	191.5	0.39	27	VL10	1.09	91.25	0.4
13	SFG1	1.98	154.5	0.38	28	VL11	1.98	133.5	0.4
14	SFG4	1.31	191.5	0.38	29	VL12	1.04	130.75	0.4
15	SFG5	1.74	155.5	0.4					

Chapter 2

Co-planar streams and pancakes

In this chapter we present the analysis done on the cold streams in the context of the cosmic web using the ART simulations. This analysis is meant to confirm the main results presented in (Danovich et al., 2012) and partially extend them. We note that the simulated galaxies in our sample have masses of around $6 \times 10^{11} M_{\odot}$ already at $z = 2$ and sometimes even greater masses, comparing this to the typical mass of a collapsing dark matter halo at this time (the Press-Schechter characteristic mass) which is $\sim 5 \times 10^{10} M_{\odot}$, this implies that these halos indeed correspond to high σ -peaks of the initial density field. More Specifically, the number of standard deviations which the critical collapse overdensity at this redshifts represents on that mass scale is $\nu = \delta_c(z)/\sigma(M) \sim 1.7$. Therefore these halos are indeed expected to be at the nodes of the cosmic web intersected by dark matter filaments containing cold streams as described in the introduction.

2.1 Cold streams identification

In analyzing the cold streams we focus on the gaseous filaments which are embedded in the DM filaments. This is more convenient in terms of the analysis since the gas, being dissipative, it will form thinner more well defined filaments compared to the thicker and less concentrated DM filaments resulting from the collisionless nature of the DM particles. We present two methods for the identification of the cold streams which we use in the analysis. The first is using the radial mass flux density per unit solid angle:

$$\frac{d\dot{M}}{d\Omega} = \rho v_r r^2 \quad (2.1)$$

Where ρ is the gas density, v_r the radial velocity and r the radial distance from the galaxy center. The choice of the mass flux is motivated by the known properties of the cold streams having a high density and a large radial velocity on the order of the virial velocity $v = \sqrt{\frac{GM_v}{R_v}}$. The mass flux is then interpolated on spherical shells at different radii and the analysis is performed on these spheres. The streams are then identified using a friends-of-friends algorithm on the spherical shell by associating neighboring gas cells above a given

influx density threshold (5-6 times the mean), to the same stream. The stream position is then set to the influx weighted average position of all the cells associated to the stream.

The second method for the identification of the streams is motivated by two main properties of the cold streams which are the anisotropic coherent geometry i.e. narrow separated filaments and being consisted of cold dense gas. For each galaxy we first focus only on the cold and dense gas which we define as having $T < 10^5 K$ and a density satisfying $100 \frac{\Omega_b}{\Omega_m} \rho_c X m_H \leq n_H < 1 \frac{H}{cm^3}$, where $\frac{\Omega_b}{\Omega_m}$ is the universal baryonic fraction, $\rho_c = \frac{3H^2}{8\pi G}$ is the critical density, X is the primordial Hydrogen mass fraction and m_H is the Hydrogen atom mass. The factor of 100 was chosen by inspection and the upper limit of $1 \frac{H}{cm^3}$ is the simulation critical density for star formation. This criteria for the cold filamentary gas was adopted from (Kimm et al., 2011) and was found visually to separate the cold streams well. We then perform a friends-of-friends algorithm on the gas cells, recording their directional cosines and joining gas cells which have directional cosines in the range of $0 - 0.3$ from the mean directional cosines of the rest of the members of the given identified stream. If a cell is not within this range, then it is considered as a part of a new stream and this process repeats iteratively. In order to reduce noise we focus on the radius range $0.5 - 2R_v$. Once the streams catalogs for each galaxy are produced, we filter them by requiring each filament to contain at least 3,000 gas cells and have a mean radial distance greater than $0.7R_v$, this additional filtering ensures that we indeed have elongated filaments and not arbitrary clumps of cold dense gas. Finally the streams are ordered by their total mass, and we record their average radial position, total mass and total AM. We demonstrate the result of this process in figure 2.1 using 3d images of one of the galaxies and its identified filaments.

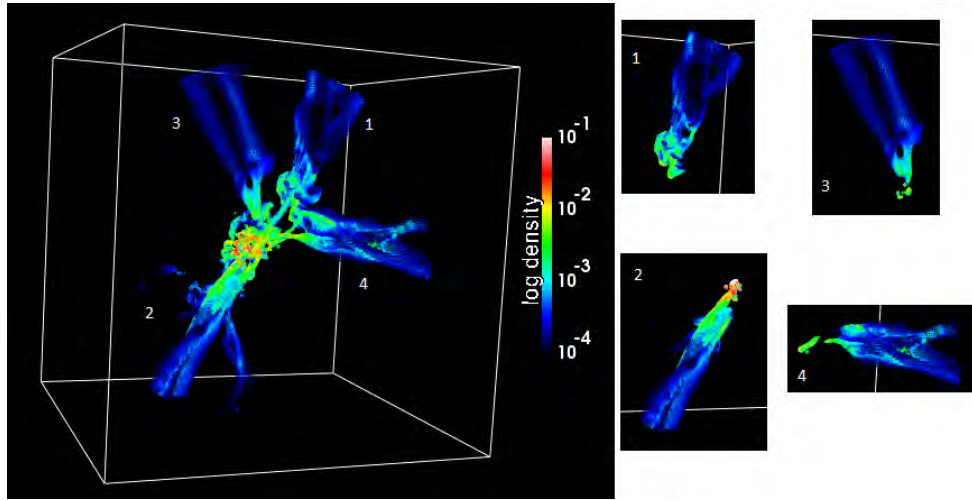


Figure 2.1: (Left) Cold dense gas in a box of side $4R_v$ for the galaxy MW3 at $a = 0.38$. (Right) the four identified filaments using the method described, showing only the cells associated with each filament.

2.2 Streams co-planarity

The main claim we want to test is whether the three major streams (if there are three, and the maximum flux is less than a factor of a 100 larger than the minimum flux) tend to lie in a plane containing the galaxy at the center. For this we examine the streams in a thick shell at $(1 - 2)R_v$ which improves the analysis by including more information and emphasizes the elongated streams. Following their identification we order them by the total influx and choose the three major streams. We then fit the position of the three streams to a plane going through the central galaxy by minimizing the sum of the squares of the angular distances along the sphere from the points to the plane. We note that three streams is the minimum number of streams for which co-planarity is not trivial.

Figure 2.2 demonstrates qualitatively the tendency for co-planarity of the streams by showing the influx in the thick shell for a sample of the simulated galaxies at different times. The figure shows the identified streams marked by green dots and the best-fit plane that was rotated to the equator. In addition to the three major streams, we see another component consisting of a gas with lower influx density of $\sim 10 - 15 M_\odot \text{yr}^{-1} \text{rad}^{-2}$ compared to the streams with $50 - 100 M_\odot \text{yr}^{-1} \text{rad}^{-2}$, which however is still higher than the average influx but more importantly also tends to lie in the same plane defined by the streams, which make the co-planarity of the streams even more significant. This extended gas which lies in the same plane defines a pancake structure around the halo. In the same figure we also show for the same galaxies the entropy maps $S = (\rho/T)^{-2/3}$, emphasizing the streams and the pancake structure as being low entropy (cold and high density) compared to the surrounding high entropy gas. Thus we see in the simulations both phases of the gravitational collapse described by the Zel'dovich approximation, namely the two dimensional collapse resulting in the dense filaments and the one dimensional collapse resulting in the lower density planar structures.

In order to test the statistical significance of the co-planarity of the streams, we compare the deviation of the streams from the fitted plane (the sum of the distances) to a random realization of three points on a sphere with the same number of grid cells and restricting the points to be farther than 30 deg from each other for a fair comparison. We use the Kolmogorov-Smirnov (KS) test which looks at the maximum deviation between the cumulative distribution functions (CDF) of the deviation from a plane, d , in the two samples, and provides a statistical measure for the likelihood that the simulation data points are taken from a random distribution. In figure 2.3 We show the CDFs of the two distributions using 437 data points from the ART simulations. The maximum vertical separation between the CDFs is $D = 0.21$ with a p value of 5×10^{-15} , confirming the results of the lower resolution simulations presented in (Danovich et al., 2012). (We note that although there is contamination from the fact that adjacent snapshots are correlated, this can have both positive and negative contribution). Another way to test the significance of the pancake structure and the planarity of the streams bringing most of the material to the forming galaxy is to examine the alignment of the stream plane (SP) and the minor axis of the moment of inertia of the material in the halo and its vicinity. The moment of inertia is defined by $I_{ij} = \sum m(\delta_{ij}r^2 - x_i x_j)$, where the sum is over all particles and the

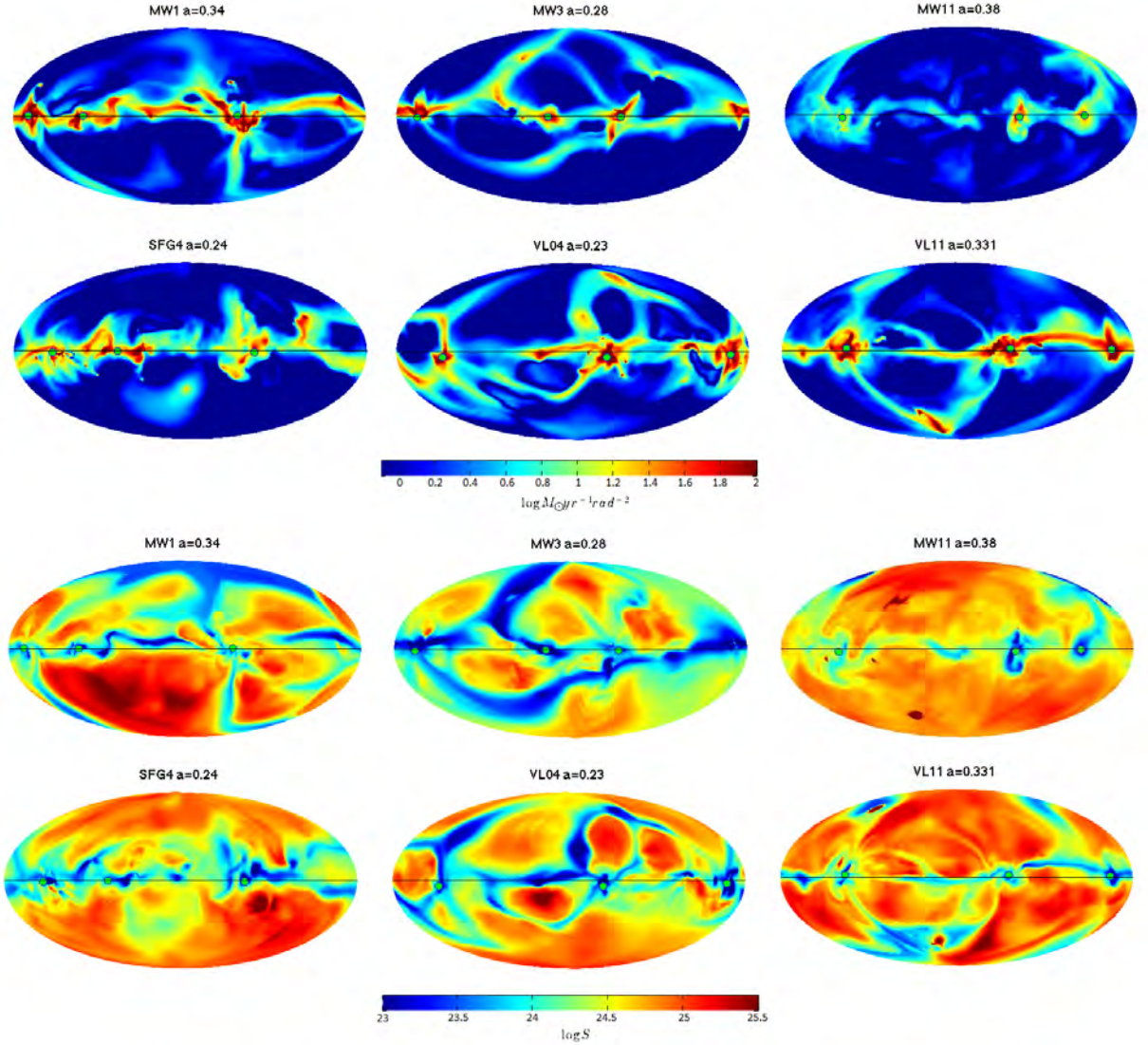


Figure 2.2: Co-planar streams embedded in low entropy pancakes in the ART simulation. Shown are all-sky Hammer-Aitoff maps of the radial influx of gas mass per solid angle (top six) and the gas entropy for six simulated galaxies. These examples show the typical scenario of 3 major streams with high influx values (red color) that lie in a great plane which includes the galaxy center, and that includes additional infalling gas with lower influx and low entropy, surrounded by a higher entropy gas with much lower influx values. The coordinates were rotated such that the best-fit plane is at the equator marked by the black line and the positions of the streams are marked by green dots.

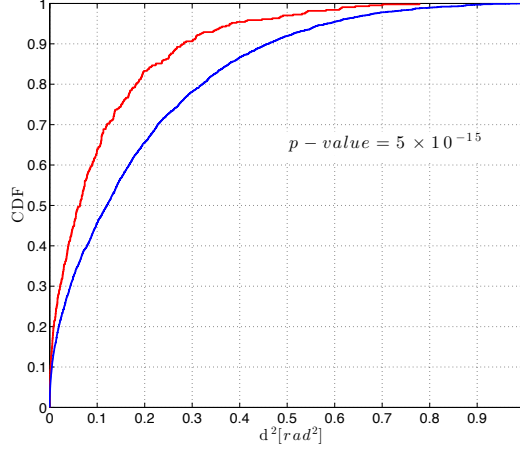


Figure 2.3: The significance of the stream co-planarity in a shell $(1 - 2)R_v$. Shown is the CDF of the deviation of the three largest streams from the best-fit plane using 437 snapshots (red) compared to the CDF of 4,000 realizations of 3 points placed randomly on a sphere (blue). The null hypothesis is rejected with a p value of 5×10^{-15} .

positions are relative to the galaxy center. The minor axis corresponds to the eigenvector with the largest eigenvalue of the inertia tensor. We use all the baryons and DM within $2R_v$ to calculate the moment of inertia tensor. In figure 2.4 we show the distribution of the cosine of the angle between the two vectors. We see a strong correlation with median $\langle \cos \theta \rangle = 0.9$, indicating the importance of these pancake structure with embedded stream for the mass distribution within the halo and outside.

2.3 Mass and AM distribution in streams

We saw in the previous section that the cold streams are characterized by high influx densities relative to the ambient gas, and thus are the primary source for cold gas supply to the central galaxy. We will see in the next chapter that the cold dense gas also has high specific AM compared to the hot gas or dark matter. It is therefore of interest to examine how these properties are distributed among the cold streams. We use the second method discussed, and measure the total mass and AM in the identified streams. Figure 2.5 shows the distribution of masses and AM within the identified cold streams. We see that there are three major streams with $\sim 90\%$ of the total mass and one dominant stream with $\sim 70\%$ of the total mass. Similarly the AM distribution shows a dominant stream carrying $\sim 60\%$ of the total AM. These results agree qualitatively with the results in (Danovich et al., 2012) for the lower resolution simulations. (Tillson et al., 2012) using tracer particles to follow individual filaments contribution to the disc, have found very similar results as can be seen in their figure 5, where a single filament out of three, dominates with $\sim 70\%$ of the mass and 75% of the AM.

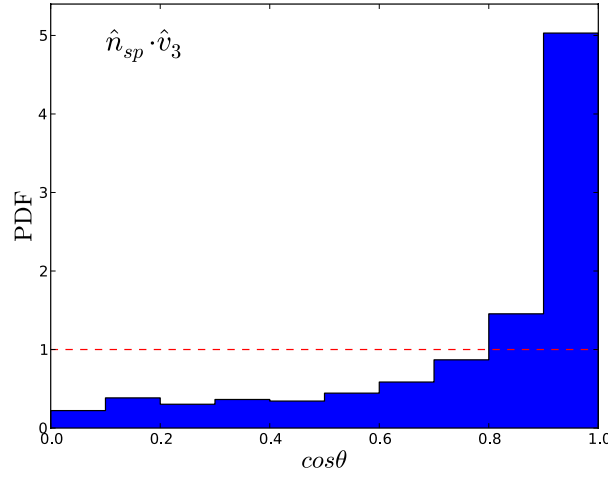


Figure 2.4: Alignment between the streams best-fit stream plane normal \hat{n}_{sp} and the minor axis of the inertia tensor \hat{v}_3 of the region $< 2R_v$. Shown is the distribution of $\hat{n}_{sp} \cdot \hat{v}_3$, for all halos and at all times. The median of the distribution is $\langle \cos\theta \rangle = 0.9$, indicating the importance of the planar structure around the halo set by the pancake and streams in determining the shape of the large scale structure material in the vicinity of the halo.

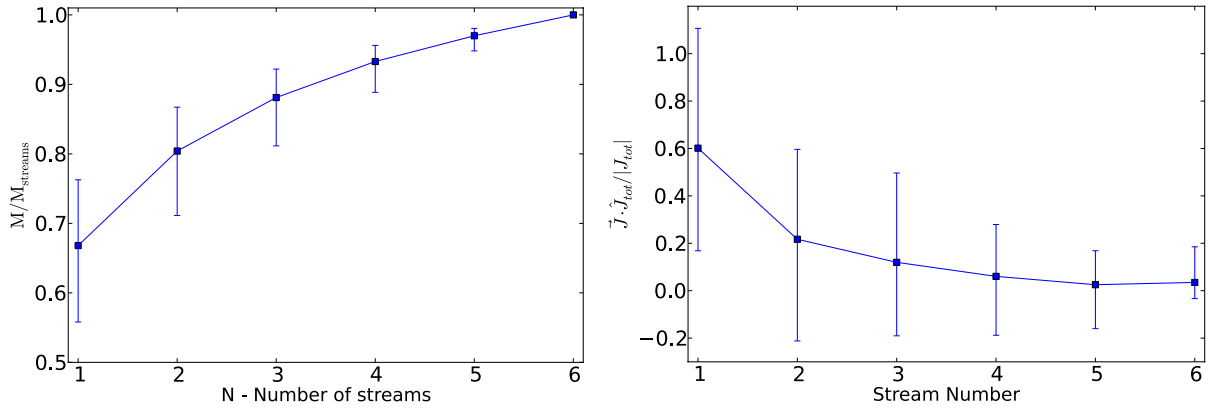


Figure 2.5: Mass and AM distribution in the cold streams. (Left) the fractional contribution of the first N streams to the total mass in streams. (Right) The AM fraction in each stream in the direction of the total AM vector and relative to the total amplitude of the AM in the streams. Shown are the mean values and standard deviations for all the simulated galaxies and at all times.

2.4 Stream plane extension, alignment and stability

As the cosmic web is 3-dimensional in nature, the planar structure will have to join in some way the large scale cosmic web. We address this qualitatively here by showing three examples of the radial evolution of the streams and the stream plane using Hammer-Aitoff projections of the density from $5R_v$ to $0.4R_v$ in figure 2.6. This shows the transition from the large scale cosmic web characterized by a complex network of sheets intersecting at the positions of the filaments. At the virial scale this network is reduced to a single dominant sheet with filaments embedded within it. The high density sheet/pancake is preserved down to $\sim 0.6R_v$ where the density of the sheet equals the mean density in the halo. Some of the filaments are seen to preserve their position on the sphere down to the inner halo. This process from the virial scale to the inner halo is demonstrated in figure 2.7 using density profiles as a function of the polar angle relative to the plane showing the high density profile of the stream plane merging with the background density of the halo. The fact that the stream plane in general doesn't penetrate all the way to the disc region, has obvious implications on the orientation of the disc plane relative to the stream plane. In figure 2.8 we show the alignments of the disc and the stream plane which are weakly correlated with a median cosine of $\langle \cos \theta \rangle = 0.61$. We also show the alignment of the AM of the three major streams with the total AM of the cold gas within the halo (the result is similar for the total AM of the DM as well) with a median of $\langle \cos \theta \rangle = 0.61$ which is a strong alignment considering these are two AM vectors and we note that these streams as described, contain cells from $0.5R_v$ up to $2R_v$. The last figure shows the alignment of the AM of the three major streams with the direction of the stream plane, with a median of $\langle \cos \theta \rangle = 0.66$, this can be understood in the case of one dominant stream determining the AM of the plane. Finally we check the relation between the disc and the AM in individual streams. In figure 2.9 we show the distribution of the cosine of the angle between the total AM direction of each stream and the disc spin axis. We see that typically one of the streams is most aligned with the disc spin axis and one that tends to be anti-aligned with the disc. Finally, in figure 2.10 we address the question of the stability of the stream plane with time by showing the median of the cosine of the angle between the normal to the fitted stream plane at each snapshot and the stream plane at the final snapshot. We see that the median is around ~ 0.75 most of the time and becomes more aligned up to > 0.9 around the final 4 snapshots. Compared to the random distribution marked by the gray dashed line, we see that the stream plane is relatively stable however there is a large scatter, part of which may be due to the method of identification of the streams, and partly due to actual reorientation of the plane and movement of the streams.

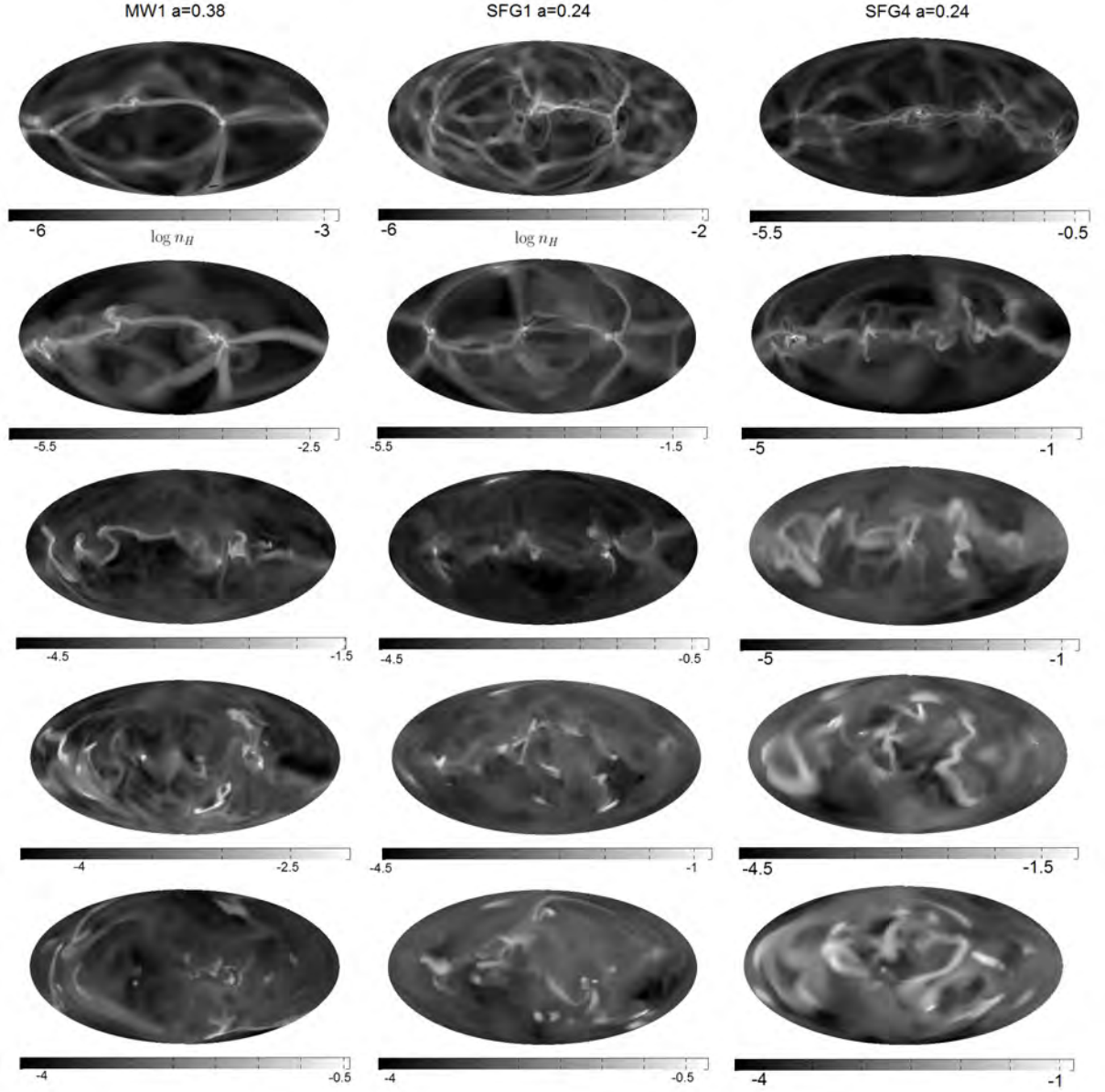


Figure 2.6: All-sky Hammer-Aitoff projections of the gas density in thin shells from top to bottom: $r = 4.9 - 5.0R_v$, $1.9 - 2R_v$, $r = 0.9 - 1.0R_v$, $r = 0.5 - 0.6R_v$, $r = 0.3 - 0.4R_v$ for MW1 at $a=0.38$ (Left), SFG1 at $a=0.24$ (Middle) and SFG4 at $a=0.25$ (Right). The projections show the transition from the large scale cosmic web $\sim 5R_v$ containing filaments found in the intersection of sheets down to the virial scale where a single dominant sheet is evident, containing three major filaments. The stream plane penetrates down to $\sim 0.5R_v$ where it is lost when the density of the plane is comparable to the ambient density.

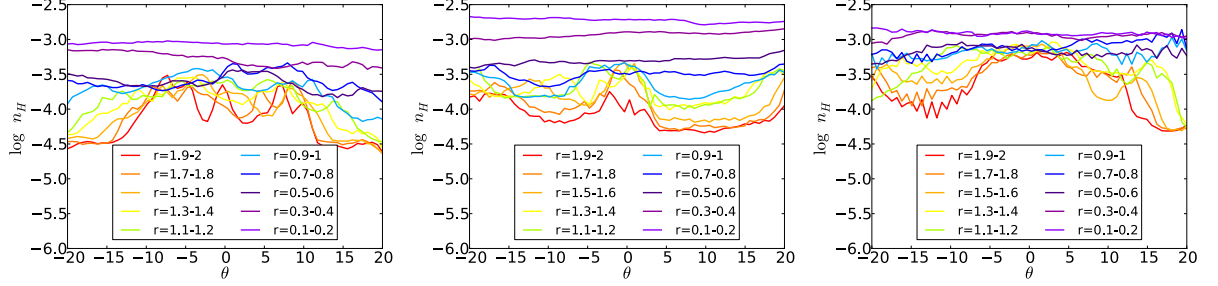


Figure 2.7: Density profiles at various radii between $0.1R_v$ to $2R_v$ as a function of the polar angle θ relative to the stream plane (at $\theta = 0$), for the three exmpales shown in the previous figure. The pancake feature is present untill the density becomes equal to the mean density at that radius.

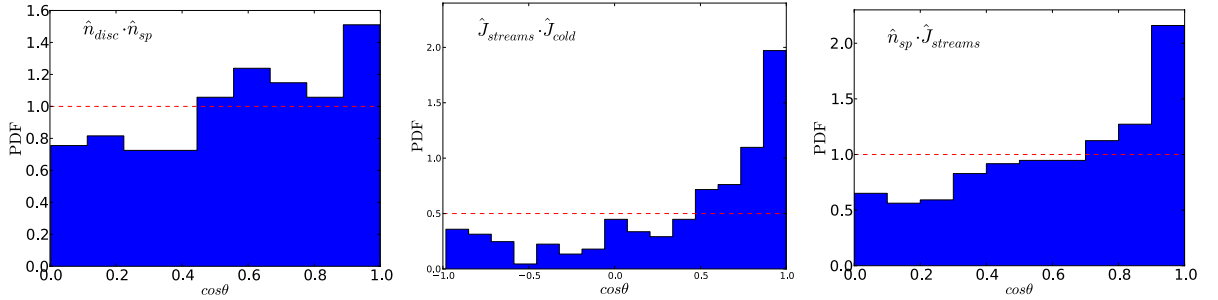


Figure 2.8: Distribution of the alignment of the disc and stream plane (Left), the AM in the three major stream with the AM of the cold gas in the halo (middle) and the AM in the three major streams with the stream plane normal. The median values of the distributions: $\langle \hat{n}_{sp} \cdot \hat{n}_{disc} \rangle = 0.61$, $\langle \hat{J}_{streams} \cdot \hat{J}_{cold} \rangle = 0.61$, $\langle \hat{n}_{sp} \cdot \hat{J}_{streams} \rangle = 0.66$.

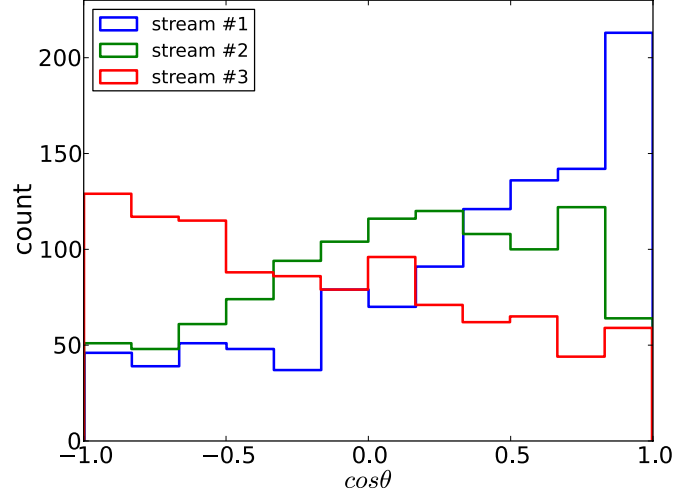


Figure 2.9: Distribution of the cosine of the angle between the total AM of the three major streams and the disc spin axis. The median values for the three streams are: 0.44, 0.14, -0.21.

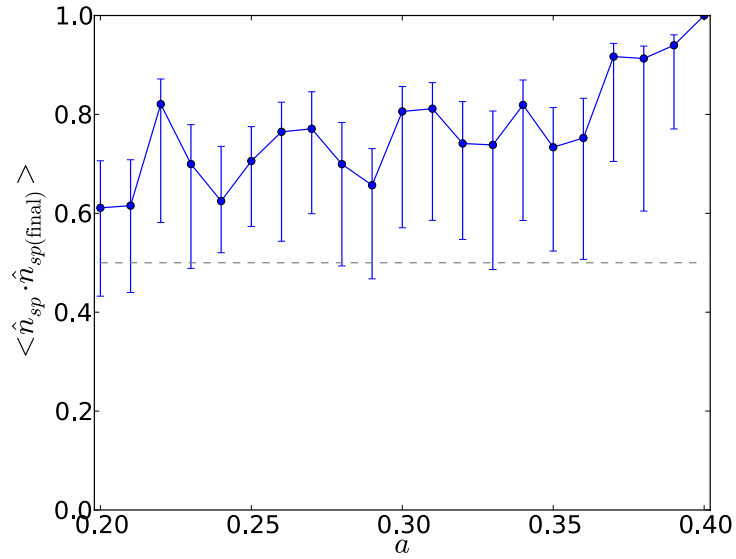


Figure 2.10: Stream plane stability with time. Shown is the median of the cosine of the angle between the stream plane at each snapshot and the final snapshot, averaged over all halos. The gray dashed line marks the value for a random distribution.

Chapter 3

AM content and transport in DM halos

In this chapter we study the angular momentum content of the different components making up the DM halo, and eventually the galaxy itself.

3.1 The spin parameter

The angular momentum J of a given component is commonly expressed in terms of the dimensionless spin parameter, introduced by (Bullock et al., 2001):

$$\lambda_x = \frac{J_x}{\sqrt{2}M_x R_v V_v} \quad (3.1)$$

Where J_x is the total angular momentum of the component x , M_x is the total mass, and R_v, V_v are the virial radius and virial velocity of the halo. The original spin parameter definition was due to (Peebles, 1969): $\lambda = \frac{LE^{1/2}}{GM^{5/2}}$ which is physically motivated, since it measures how rotationally supported a system is. This can be understood by deriving the definition from the ratio of the centrifugal v^2/r and the gravitational GM/r^2 accelerations. The two parameters are identical for an isothermal sphere, but in general differ by a numerical parameter depending on the density distribution within the halo. For convenience of computation we use the first definition. Numerical studies of the spin parameter of dark matter halos have found it to follow a log-normal distribution with weak dependence on mass and time, and a median value of $\lambda \sim 0.04$.

$$P(\lambda) = \frac{1}{\lambda\sqrt{2\pi}\sigma} \exp\left(-\frac{\ln^2(\lambda/\langle\lambda\rangle)}{2\sigma^2}\right) \quad (3.2)$$

In figure 3.1 we show the measured probability distribution of the spin parameter of four different components within the simulated DM halos: cold gas ($T < 10^5 K$), hot gas ($T \geq 10^5 K$), all baryons (gas and stars) and dark matter. We note that an alternative definition for the hot gas can be using $T_{shocked} = 3T_v/8$ as the limit, especially at later times this value can be higher than $10^5 K$. As in the previous chapter, for the cold gas we use the additional density criteria to select the filamentary cold gas. Within the halo, the dense

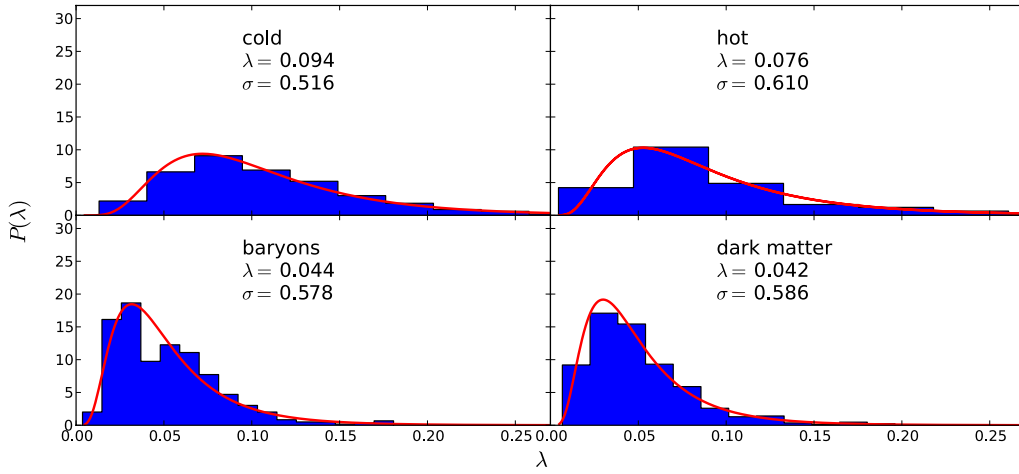


Figure 3.1: Spin parameter distributions for cold gas ($T < 10^5 K$), hot gas, baryons and dark matter within R_v , fitted to a log-normal distribution.

component makes 80% and above in terms of mass. The main difference is outside the halo where the dense component is $\sim 60\%$, and we thus avoid the cold diffuse gas in this way. We fit the distributions to a log-normal distribution as expected for the DM component. We see that the cold has the highest spin parameter with $\lambda_{cold} = 0.094$ and $\sigma = 0.516$, compared to the baryons and DM which have comparable spin parameters $\lambda_{baryons} = 0.044$ and $\lambda_{DM} = 0.042$. In figure 3.2 we show the evolution of the spin parameter of the different components with time within the halo and within $0.1R_v < r < 1R_v$ (excluding the disc region). The DM has a constant spin parameter as expected, with little variation. Mergers are known to cause sharp increases and declines in the DM spin parameter, but these are apparently smoothed out when averaged over a large sample, as is the case here. The baryons as a whole follow very closely the DM component as is usually assumed following tidal torque theory (TTT) and the idea that both are acted on by the same torques prior to virialization. When excluding the disc region we see that the baryons no longer follow the DM and have a higher specific AM since in this case they are not mixed with the previously collapsed lower specific AM material. The gas components show some evolution with time. Most apparent is the evolution of the cold gas component, which shows a steady increase in the spin parameter with time, and has the highest average spin parameter. From (3.1), $j = \sqrt{2}\lambda R_v V_v$, a constant or increasing spin parameter indicates that the total specific AM of all components increases with time according to the evolution of the virial quantities. The increase in specific AM is also consistent with the picture from tidal torque theory where the transported material into the halo had more time to experience the surrounding torques from the environment and having larger inertia tensor values, result in the increased AM. The clear distinction between the cold gas and DM behaviours has to do with the fact that the DM within the halo keeps building up and doesn't collapse towards the center but contains particles with orbits which return to the outer halo region, thus its AM is

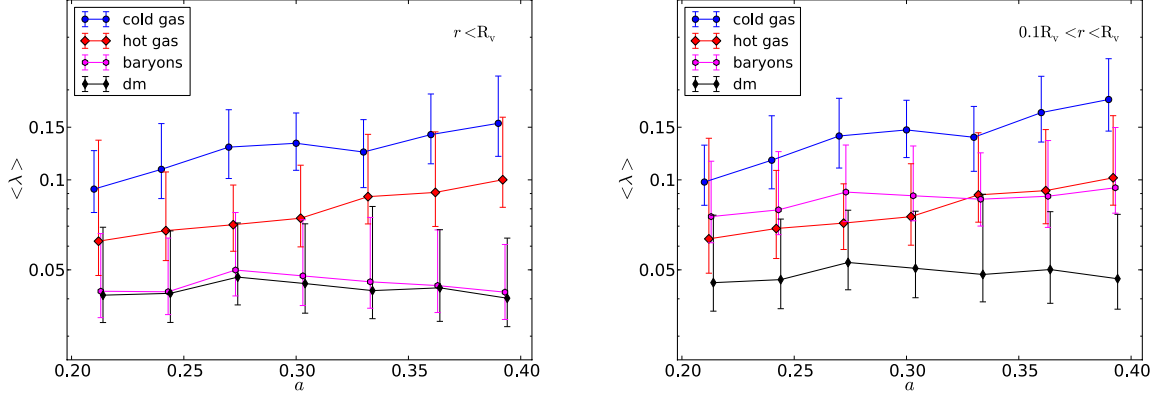


Figure 3.2: Evolution of the spin parameter of the different components in the DM halos. Shown is the spin parameter vs. expansion factor for cold gas, hot gas, baryons and DM within $r < R_v$ (Left) and $0.1R_v \leq r \leq R_v$, averaged over all halos in the sample. (The data points were shifted with respect to each other for clarity).

built during the entire history of the halo and has contribution from DM particles that were accreted during this time, which includes both low AM particles and newly accreted higher AM particles. This is also partially true for the baryons as a whole, however part of which cools and collapses towards the disc since it can radiate its energy, and therefore at later times the halo will contain relatively newer gas that came with higher specific AM as seen in the right figure for the baryons. This is even more significant in the cold gas case, since it doesn't suffer from shock heating and can reach the disc region much quicker without getting mixed in the outer halo, and thus the outer halo will mostly contain newly accreted cold gas with higher specific AM. The increased separation of the cold gas from the baryons as time increases can also be attributed to the increased cooling times as the virial mass of the halos increases which results in more mixing at later times also for the baryons. In a following section we will try to quantify this idea of mixing vs. coherent accretion. The lack of time evolution and mass dependence of the spin parameter of the dark matter component seen in the figure can be derived in general from TTT using simple scaling relations. The angular momentum of the dark matter halo (or each collapsing shell) is set according to TTT at turn around and can be written as:

$$J \sim a^2 \dot{D} \nabla^2 \phi_0 M R_0^2 \quad (3.3)$$

For an EdS universe which is a good approximation at the relevant times here, the expansion factor and the linear growth of density fluctuation are $a(t) \propto t^{2/3}$ and $D(t) = a(t)$, therefore $a(t)\dot{D}(t) \propto t = a^{3/2}$. Turn around can be approximated as the time when the overdensity becomes ~ 1 , and the density is related to the gravitational potential through the Poisson equation $\delta \sim D(t)\nabla^2 \phi_0$, setting $\delta = 1$ we get: $\nabla^2 \phi_0 \sim D(t)^{-1} \sim a(t)^{-1}$. The co-moving radius is determined from $R_0^3 \bar{\rho}_0 \sim M$, therefore $R_0 \sim M^{1/3}$. We get the expression

for J in terms of a and M :

$$J \sim a^{1/2} M^{5/3} \quad (3.4)$$

Next we need to find expressions for the physical radius and the virial velocity in the definition of λ . The physical radius satisfies $\rho R^3 \sim M$ and the density scales as $\rho \sim \rho_0 a^{-3}$, therefore

$$R \sim a M^{1/3} \quad (3.5)$$

The virial velocity is defined as $V_v = \sqrt{\frac{GM}{R}}$ and therefore scales with mass and time as:

$$V_v \sim M^{1/3} a^{-1/2} \quad (3.6)$$

Plugging the last three expressions into the spin parameter $\lambda \sim \frac{J}{MR_v V_v}$ gives $\lambda \sim a^{1/2} M^{5/3} M^{-1} a^{-1} M^{-1/3} M^{-1/3} a^{1/2} = \text{const.}$

We look at the mass and time dependence of the spin parameter distributions of the different components within the halo in more detail in figure 3.3 by fitting the distributions for different redshift ranges $4 < z < 2.5$ and $2.5 < z < 1.5$ and different halo mass ranges $M < 10^{11.6} M_\odot$ and $M \geq 10^{11.6} M_\odot$. This again shows that the redshift and mass dependence of the DM and baryons as a whole spin parameters is small compared to that of the cold and hot gas, which show a significant increase both with time and halo mass. Also, we see that the spin parameter of the DM and all baryons seems to decrease with increasing mass which is opposite of the behavior of the cold and hot gas which increase their spin parameter. By performing the same analysis on the gas alone, we get a similar behavior to that of the cold/hot gas, we therefore conclude that the reason for this behavior in the baryons is due to the stars contributing small angular momentum for a given mass. One source of stars other than the disc, is through merging satellites, which are present in smaller dark matter halos. Therefore it is possible that the satellites in the more massive halos bring stars and DM with less specific AM, possibly due to more radial orbits in the more massive halos. In figure 3.4 we show the radial profiles of the spin parameter in thin shells for the different components from $r = 0.1R_v$ to $r = 3R_v$ at three snapshots $z \sim 3.5, 2.5, 1.5$ where each redshift bin contains actually 3 snapshots of the adjacent redshifts. We see that the cold gas has a significantly higher spin parameter and correspondingly higher specific AM in all radii, i.e. both within the virialized halo and accreting into the halo beyond the virial radius compared to the rest of the gas and the DM. We note that using only the infalling ($V_r < 0$) particles/gas cells gives qualitatively similar results. Within the halo, the dark matter component spin parameter is highly reduced, however beyond $\sim R_v$, the DM component increases more steeply and it follows the accreting baryons more closely. This difference between the inner and outer parts is due to the virialization and mixing of the DM component taking place within the virial radius (in principle the mixing can occur at larger radii), leading to a high degree of cancellation and a lower total specific AM. We show here in addition the total cold gas component ($T < 10^5 K$) without the density criteria, we see that the two match within the halo, however differ

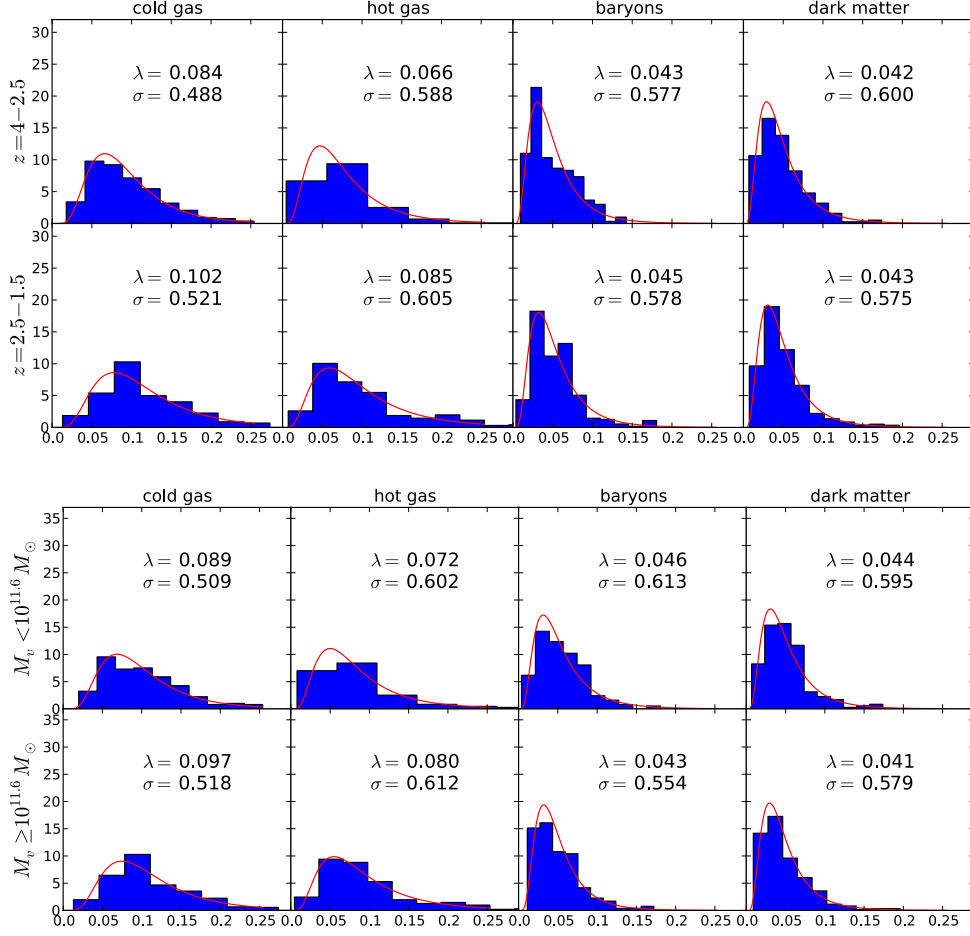


Figure 3.3: Spin parameter distributions for the different components at different redshift ranges (Top) and different halo mass ranges (Bottom). The columns correspond to the different components, and the rows to the different ranges of z or M_v .

outside. As we go to larger radii the difference between the components reduces and they follow a similar profile. This is also true for the cold gas and partially for the cold dense gas at earlier times, but not at late times where there is a difference even at high radii. This behavior at larger radii can be understood in the form of torques acting on the different components as described by tidal torque theory leading to similar spin parameters, with the later differences originating from the mixing processes described. Focusing on the accreting material at the virial radius, the fact that the spin parameters at the three snapshots are approximately equal and slightly increasing for the cold gas, indicates as was seen before for the halo as a whole, that the specific AM of the accreting material increases with time. The result that material accreting at later times has a higher specific AM is also obtained in (Pichon et al., 2011), who attribute this to an increase in the impact parameter of the filaments bringing in the material. The increase in the impact parameter is hypothesized to originate from the large scale motion of asymmetric voids that push the gas, resulting

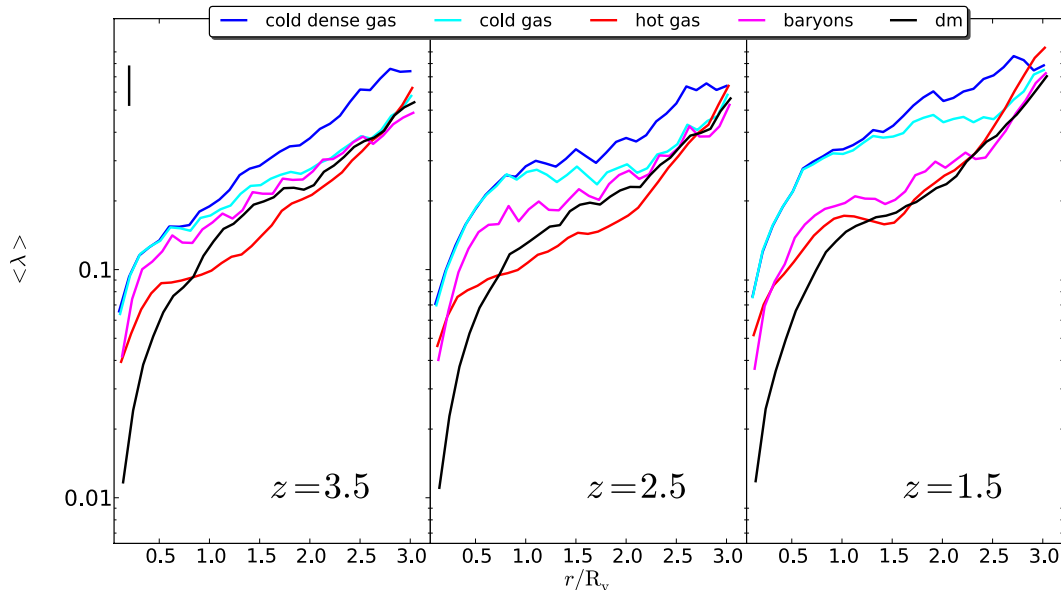


Figure 3.4: Spin parameter radial profiles ($0.1R_v - 3R_v$) in thin shells of thickness $0.1R_v$ at 3 different redshift snapshots $z = 3.5, 2.5$ and 1.5 , averaged over all halos. The errorbars were suppressed for clarity, and a sample errorbar is shown in the top left.

in residual sideways motion increasing the impact parameter. Another implication of the growth of accreting AM with time as also pointed out in (Pichon et al., 2011) is regarding the growth of the disc galaxy being an inside-out process since gas reaching at later time with higher AM will reach farther radii of the galaxy. As time increases from left to right in the figures, we see that the separation of the cold gas from the other components also increases. As before, this is attributed to the combination of increased transported AM together with increased mixing with older material having lower specific AM and longer cooling times due to increase halo mass, reducing the specific AM of the baryons and the DM. Finally, we see that the cold gas and baryons spin parameter is reduced at the disk region ($0.1R_v$) to $\lambda \sim 0.05$ which is similar to the total DM halo spin parameter which in turn is used to model the disc radius assuming conservation of AM during the collapse to form the disc. An important result due to (Bullock et al., 2001) is that there exists a power law relation between the spin parameter (which is equivalent to the specific AM) of each spherical shell and the radius, for the DM they obtained $j \propto r^{1.1 \pm 0.3}$. We show this in figure 3.5, which is similar to figure 3.4 only here we plot both axis on a log scale, and fit the profiles up to the virial radius to a straight line. We see that the profiles of all the components can be fitted relatively well to a straight line indicating a power law $\lambda \propto r^\alpha$, and the DM component has $\alpha \sim 1.1$ in agreement with the cited result. The other components have a relatively smaller value for α , with the cold and hot gas behaving most differently to the DM and baryons as a whole. The power law result in principle can be

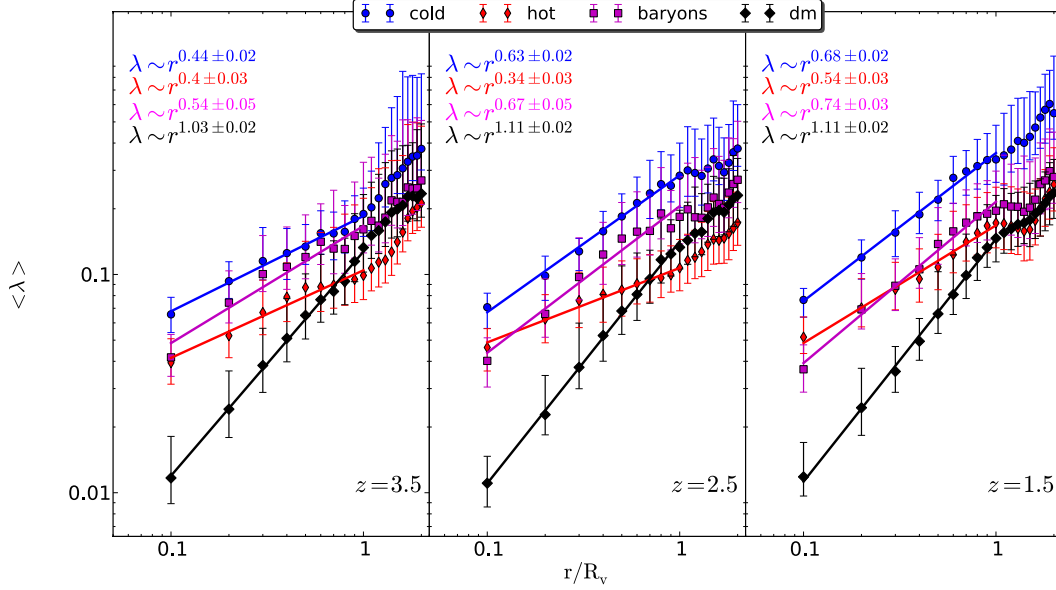


Figure 3.5: Spin parameter radial profiles ($0.1R_v - 2R_v$) as in figure 3.4, on a log-log scale with each component fitted to a straight line in the range $0.1 - 1R_v$.

obtained from TTT, as shown in (Bullock et al., 2001), starting from a modified relation for the AM growth $j \propto D(t_c)^{3/2} \sigma(M) M^{2/3}$, where t_c is the turnaround time of a given shell (when it separates from the Hubble expansion), $\sigma(M)$ is the rms density fluctuations on the scale M . Using this relation for each shell, the radial profile for the halo is built. The turn around time for each shell is determined from the mean density fluctuation on this scale $\bar{\delta}(M)$ and is approximately when $\bar{\delta}(M) D(t_c) \sim 1$. Therefore $D(t_c)^{3/2} \sim \bar{\delta}^{-3/2}$. Using a power law power spectrum of density fluctuations $P(k) \sim k^n$ where k is the wave number, one has for the rms density fluctuations $\sigma(M) \propto M^{-(n+3)/6}$ (using $M \propto R^3$). Finally using the result due to (Dekel, 1981) for the density profile about a random point in a random Gaussian field $\delta(r) \propto \xi(r)$ where $\xi(r)$ is the linear two-point correlation function, which is just the Fourier transform of the power spectrum, gives $\delta(M) \propto M^{-(n+3)/3}$. Using the relations for σ and δ in the expression for j we get $j \propto M^{2/3+(3+n)/3}$. For massive galaxies the typical value of n is between -2 and -1, leading to $j \propto M^\alpha$ with $1 < \alpha < 4/3$ in accord with the fitted result. This can in general be translated to a dependence on r , depending on the mass profile of the halo. For an isothermal sphere which is an approximation for the DM, $M(r) \propto r$, however this is not necessarily true for the baryonic components which can have a more complicated relation. From our check, the cold gas for example, when fitting the mass vs. radius to a power law, the typical coefficient is around 1, therefore for a given choice of n we can't reconcile both profiles of j vs. r , indicating a different profile build up for the cold gas compared to the DM. Finally we note, that in this log-log plot the sharp drop in the cold gas is not evident as much, however looking at the points

above $\sim 0.5R_v$ (which are closer together in this plot) we see they systematically deviate from the fitted line in the three snapshots. This is also seen for the baryons as a whole. In principle one can look at the previous profile plot and contrast where the sharp drop begins compared to the DM line, since the DM fits the power law best within the halo, and if the other components also have a simple power law they will be simply shifted vertically but not horizontally.

3.2 Kinematics and coherence

The previous sections have shown that the baryonic components and the DM can have significantly different specific AM both within the halo and outside. In this section we characterize the properties of the different components relevant for understanding these differences. The angular momentum of a single particle about a given point is determined by its total velocity v and impact parameter b relative to this point, $J = mvb$. In figure 3.6 we show the total velocity and impact parameter for the different components averaged over all the particles (with $V_r < 0$) at two different regions: the halo $0.1R_v < r < 1R_v$, and outside $R_v < r < 2R_v$. From these we see that the cold gas is characterized by a high total velocity relative to the other components within the halo and a velocity comparable to that of the DM in the outer regions. The high velocity of the cold gas within the halo can be attributed to the fact that the cold gas accelerates towards the center and stays in the center, whereas the DM and other components have more complicated orbits which go outwards and return reducing the mean infalling velocity. On the other hand, the mean impact parameter of the cold gas is relatively small at $\sim 0.3R_v$ compared to the other components which have comparable impact parameters. In the outer regions in which the components accreted into the halo, we first see that average impact parameter is increasing with time for all components, in accordance with the growth of the accreted AM. An impact parameter of $\sim 0.3R_v$ with a velocity of $\sim 1.4V_v$ corresponds to a spin parameter of a typical stream is $\lambda_{stream} = 0.3 \times 1.4 / \sqrt{2} \sim 0.3$, which we indeed find for our filaments as a typical value. Combining these two plots gives the average specific AM per particle in the different components. In figure 3.7 we show the mean specific AM in the two regions of the different components. From this we see that on a particle-by-particle basis the specific AM of the different components are quite similar in both regions, which is a result of the combination of lower impact parameter with high total velocity. As such, these results do not explain the apparent significant differences in specific AM of the cold gas vs. the other components as a whole. Since the AM is a vector quantity, the total AM of a collection of particles is affected by the way in which the AM vectors of the different particles add, or the coherence of the AM addition. We quantify the coherence of the AM addition in the different components using the following parameter for each component:

$$c = \frac{\sum_i \Theta(\vec{J}_i \cdot \hat{J}_{tot}) \vec{J}_i \cdot \hat{J}_{tot}}{J_{tot}} \quad (3.7)$$

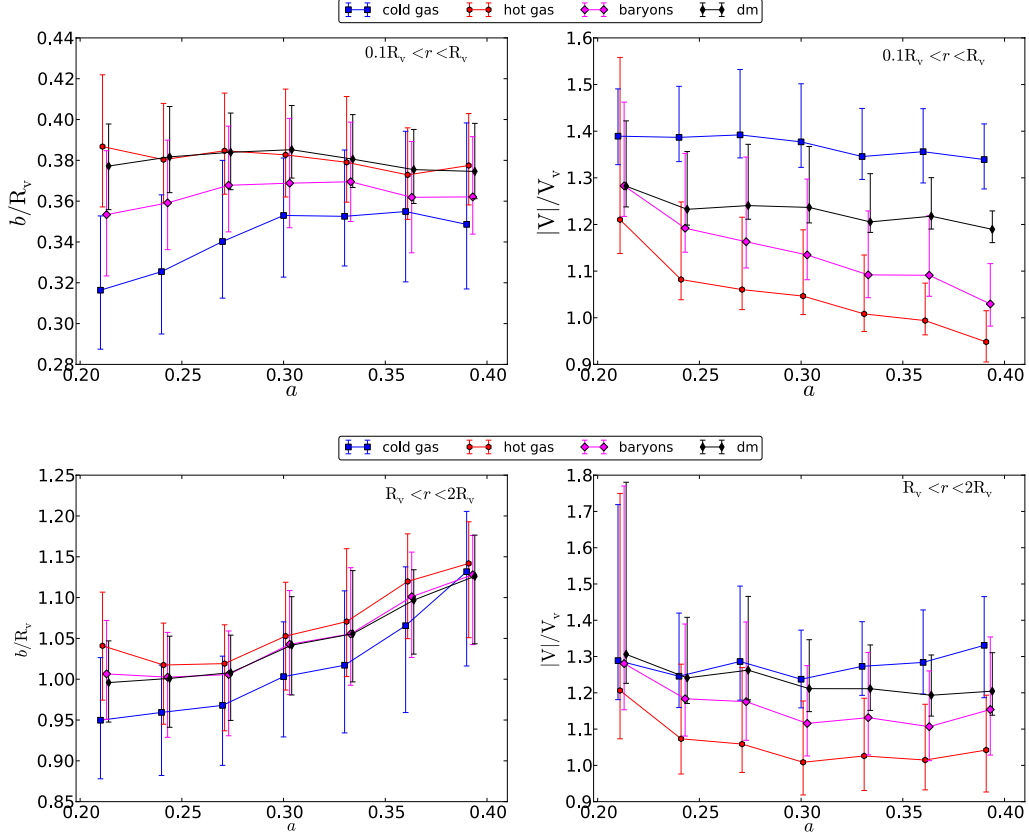


Figure 3.6: Kinematical parameters for the different components in two regions: $0.1R_v \leq r \leq R_v$ (Top), $R_v \leq r \leq 2R_v$ (Bottom) restricted to infalling particles. Shown are the mean impact parameter b/R_v (Left) and mean total velocity (normalized by the virial velocity) (Right) averaged over all infalling particles/cells and then over all halos as a function of the expansion factor.

where Θ is the Heaviside function. This parameter measures the contribution from the positively contributing particles to the total AM of a specific component, normalized by the total AM of that component. This will always be greater or equal to 1, and the closer to 1 this parameter is, the more coherent is the addition of AM. A high value of c on the other hand implies a high degree of cancellation of the AM of different particles within the component and thus a smaller coherence. An additional measure of coherence is simply the mean cosine of the angle between the different particles/cells of each component and the total AM vector of that component. In figure 3.8 we show the coherence parameter averaged over all halos as a function of the expansion factor, for the previous two regions. We see that the cold gas component has a smaller value for this parameter in both regions and at all times which implies less cancellation in the AM addition and a higher coherence compared to the other components. Similarly for the cosine of the angle between the AM vectors, we see a higher mean value for the cold gas, and also the mean value increases with

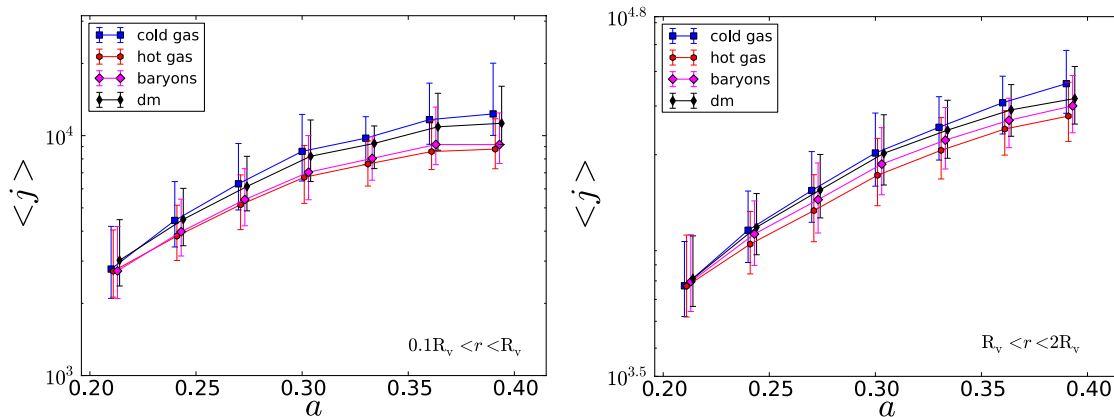


Figure 3.7: Specific AM of the different components in two regions: $0.1R_v \leq r \leq R_v$ (Left), $R_v \leq r \leq 2R_v$ (Right) restricted to infalling particles. Shown is the mean specific AM averaged over all infalling particles/cells and then over all halos as a function of the expansion factor.

time indicating an increase in the coherence of the AM of the old and new accreted cold gas, compared to a constant low value for the DM, and a much more slowly increasing mean value for the baryons and hot gas. This increased coherence in the cold gas component also helps to explain the increased spin parameter and increased separation of the cold gas spin parameter we saw previously. For the DM component we also see again the difference between the halo region and outside the virial radius. The DM is more coherent outside the virial radius and behaves similarly to the baryons and the hot gas compared to inside the virial radius where the DM is least coherent due to the high degree of mixing occurring there. The high values we see for the DM indicate a high degree of cancellation, this indicates that a significant amount of the DM has a negative AM component in the direction of the total AM of the DM in the halo. The notion of negative contribution to the AM was ignored in the study by (Bullock et al., 2001), it is therefore of interest to examine what is the fraction of mass having negative AM relative to the total AM component. We show this in figure 3.9 as a function of time averaged over all halos both within the halo and outside. We see that $\sim 42\%$ of the DM mass within the halo has negative AM, compared to only 25% for the cold gas. For the cold gas within the halo we also see that the mass fraction decreases with time from $\sim 30\%$ to $\sim 20\%$, which is again due to the short time it takes the cold filamentary gas to reach the inner regions, resulting in more correlated gas within the outer halo. Outside the halo the values increase but the cold gas still has the lowest mass fraction of negative AM. The fact that disc galaxies do not contain in general material with negative specific AM together with the fact that the mass fractions of negative AM material are not negligible, already puts in question the common assumption of conservation of AM during the disc formation, if the AM distribution of the disc is to reflect that of the baryons in the halo. One possibility is that the negative AM component plays a role in the formation of a bulge by combining with similar amounts of

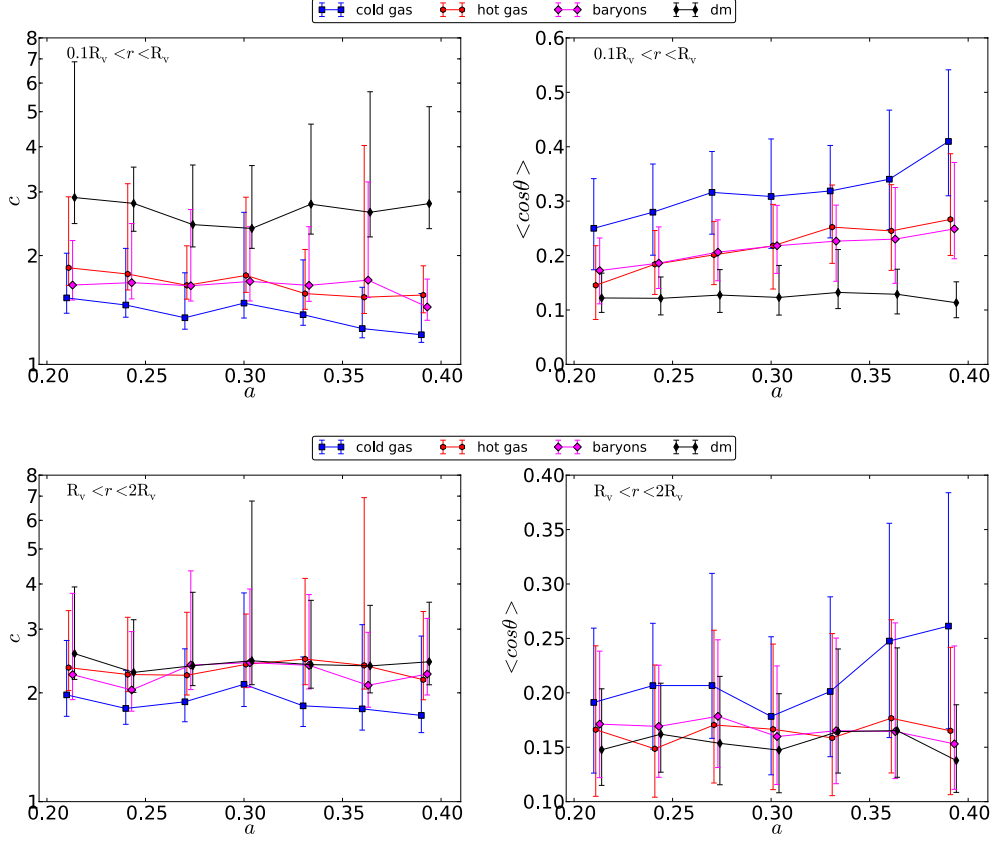


Figure 3.8: Coherence parametrs for the different components in two regions: $0.1R_v \leq r \leq R_v$ (Top), $R_v \leq r \leq 2R_v$ (Bottom) restricted to infalling particles. Shown are the mean coherence parameter c (left) and $\hat{J} \cdot \hat{J}_{tot}$ for each component (Right), averaged over all infalling particles/cells and then over all halos as a function of the expansion factor.

positive AM material. Two additional parameters we use to address the question of the coherence of the different components are the dispersion in the total velocity (in km/s) σ_v and the dispersion in the velocity direction relative to the radial direction σ_θ . The second parameter is measured by calculating the dispersion in the quantity $\hat{V} \cdot \hat{r}$. For both parameters, low values indicate less dispersion which indicate a more ordered motion. The mean values of these parameters as a function of time in the two regions are shown in figure 3.10. We see in both region the cold gas component having the smaller values, especially for the dispersion in the direction. The dark matter component behaves most differently between the two regions, with a high dispersion within the halo but a lower dispersion outside the virial radius. In terms of the velocity dispersion, the cold gas also has the lowest value, however in this case the DM has similar dispersion. We conclude this section by showing some specific examples of galaxies, highlighting the features of coherence in the AM of the different components. Figures 3.11, 3.12 and 3.13 show density and AM projections in the direction of the disc spin axis for SFG1 at $z=3.17$, MW8 at

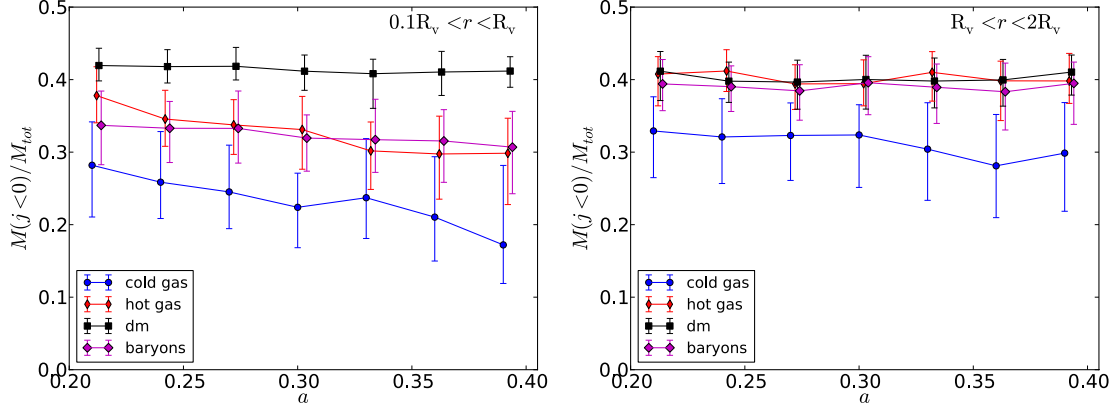


Figure 3.9: Mass fractions of material with negative AM relative to the total for the different components in two regions: $0.1R_v \leq r \leq R_v$ (Left), $R_v \leq r \leq 2R_v$ (Right) restricted to infalling particles and averaged over all halos as a function of the expansion factor.

$z=2.33$ and MW1 at $z=1.5$, covering a wide range of redshifts. The projections are of size $4R_v$ and thickness $2R_v$, and the virial radius is marked by the white circle. The top figures show the density projections and compare the distributions of the different components: baryons (gas+stars), cold gas, hot gas and DM. The baryons and the DM have similar spatial distributions outside the virial radius, with the gas basically following the DM. The cold gas on the other hand is characterized by narrow dense filaments which enter the halo and reach the inner halo almost unperturbed. The DM component is characterized by much thicker filaments in which the gas filaments are embedded. The DM also has an unordered distribution outside the halo outside the filaments, and a highly unordered distribution within the halo. The diffuse hot gas is distributed mainly in an unordered way in both regions. The bottom figures show the projected AM in the direction of the total AM of each component ($\vec{j} \cdot \hat{j}_{tot}$) within the halo (excluding the disc region $r < 0.1R_v$). The projections show the log of the AM relative to the mean and therefore shows only positive contribution to the total AM. Therefore by comparing the density projections and the AM projections, parts which show up as black in the AM projections are negative contribution to the total AM of the component. These emphasizes the difference in coherence of the AM addition between the different components. The cold gas has positive contribution to the total AM from a number of coherent streams, with all the gas cells in the stream contributing positively to the total AM. We see that not all the streams are necessarily correlated in terms of their AM and can have both positive and negative contribution, with typically one of the streams being dominant. The hot gas which is distributed throughout the entire region in an unordered way has similar positive and negative (dark regions) to the total AM of the hot component indicating a high degree of cancellation both in the halo and outside. For the DM, the dominant contribution comes from the filaments and specifically the one that contains the dominant cold stream, however there is both positive and negative contribution coming from the non-filamentary DM outside the halo, leading

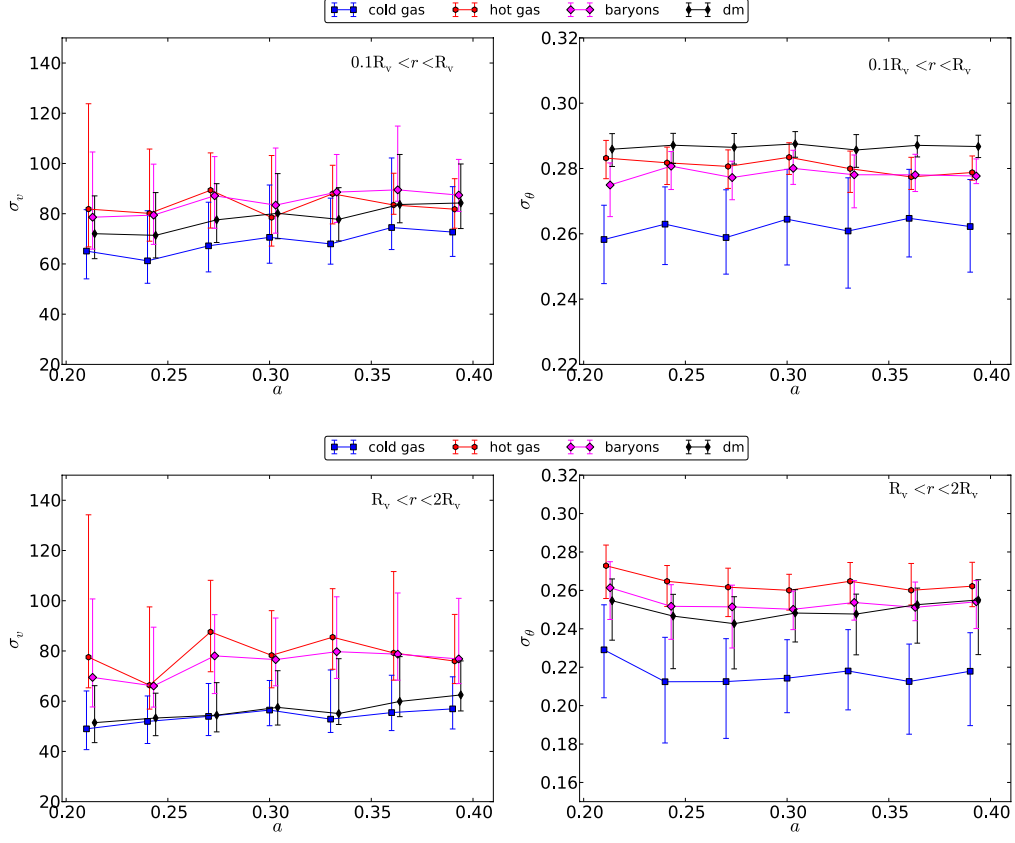


Figure 3.10: Dispersion parameters for the different components in two regions: $0.1R_v \leq r \leq R_v$ (Top), $R_v \leq r \leq 2R_v$ (Bottom) restricted to infalling particles. Shown are the dispersion in the velocity σ_v (left) and the dispersion in the velocity direction relative to radial for each component (Right), averaged over all halos as a function of the expansion factor.

to AM cancellation outside the halo and within the halo due to mixing. From the cold gas projections we also see that the gas within the halo being along the filaments is clearly related to the material that will enter the halo in the future and thus will lead to a higher specific AM with time and a higher spin parameter as seen. On the other hand, the hot gas and DM have a less correlated behavior within the halo leading to a lower spin parameter and a weaker evolution with time. We supplement these projections with the distribution of the cosine of the angle between each cell or particle AM and the total AM of that component. This is shown in figure 3.14 where we can see that the distribution of the cold gas is different than the other components which are quite similar. The cold gas has high peaks at positive values contributed from the streams, and small contribution from cold gas with negative AM relative to the direction of the total.

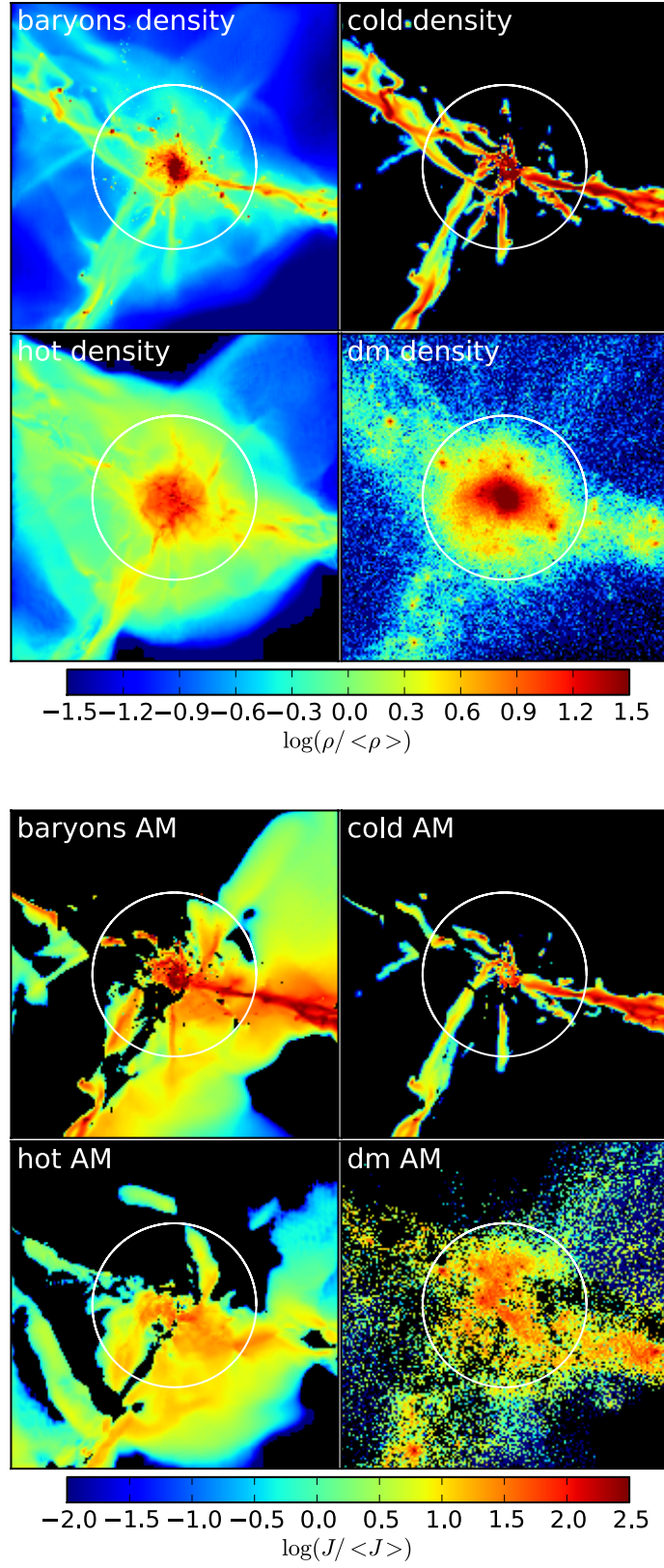


Figure 3.11: Projection maps of SFG1 at $z = 3.17$ showing baryons, DM, cold gas and hot gas density (Top) and $\vec{J} \cdot \hat{J}_{total}$ - AM in the direction of the total AM of each component within $0.1R_v < r < R_v$ (Bottom). The maps size is $4R_v$ and thickness $2R_v$ along the disc spin axis. The white circle marks the virial radius.

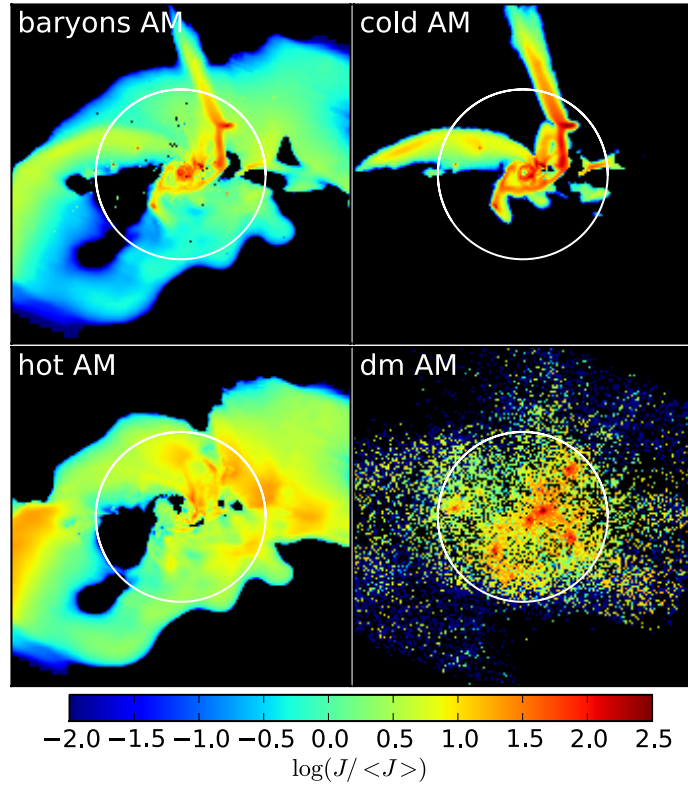
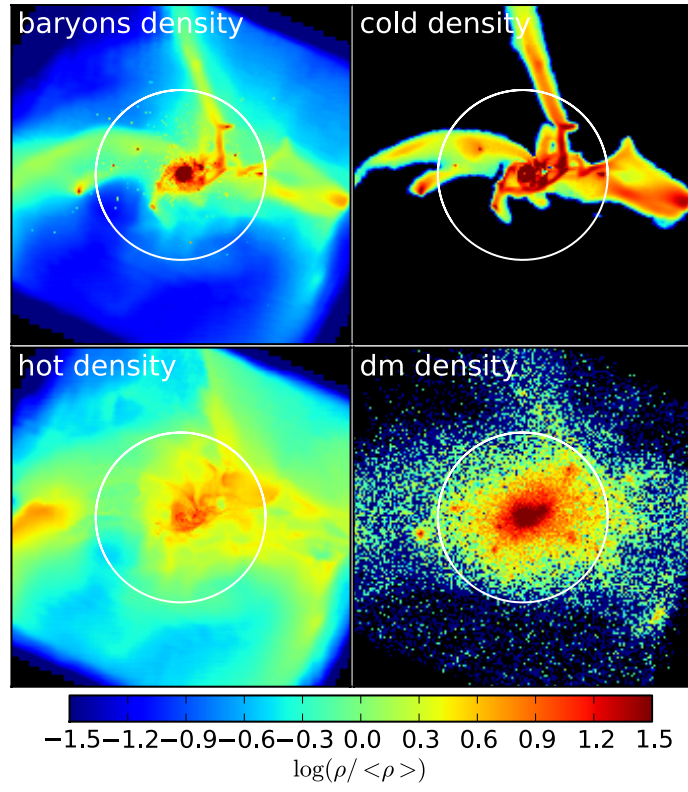
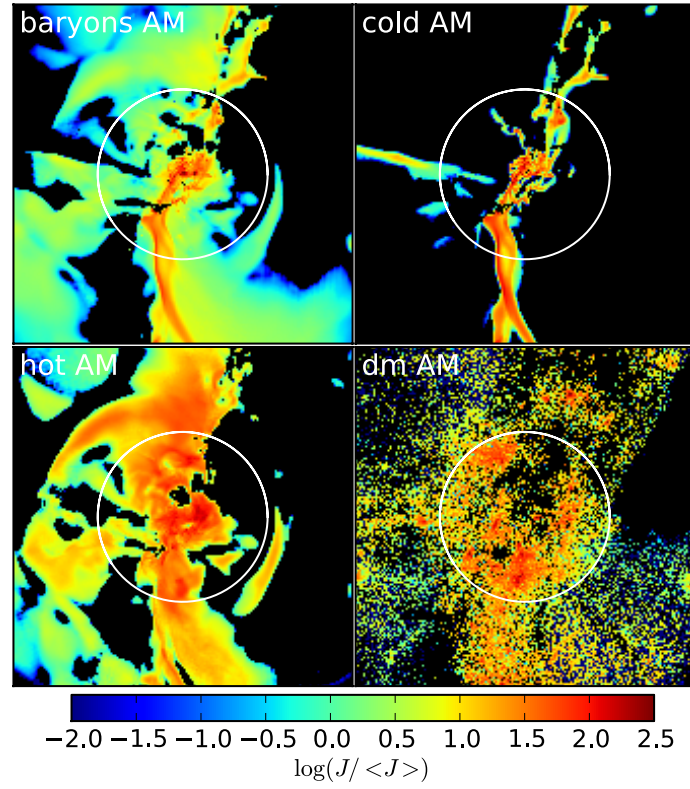
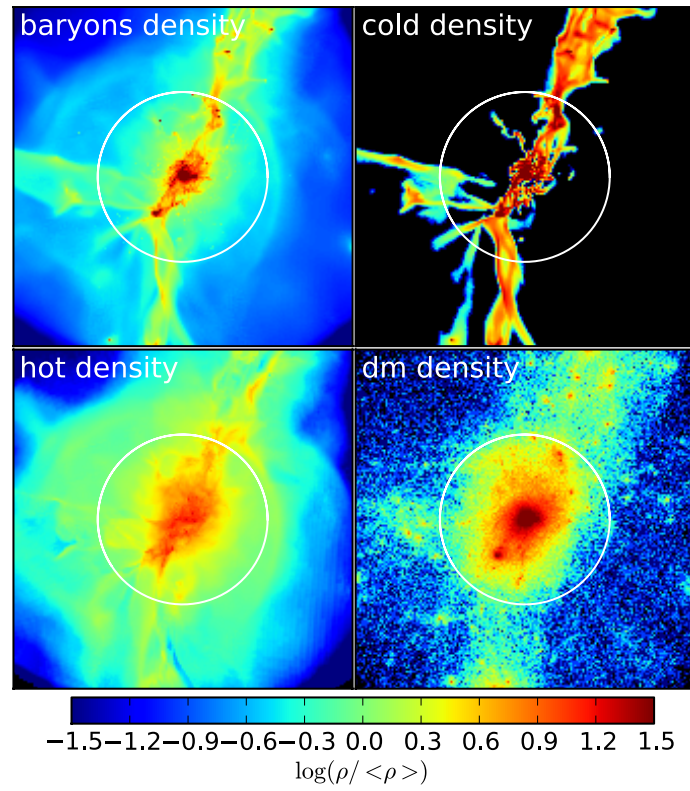


Figure 3.12: Same as figure (3.7) for MW8 at $z=2.33$.

Figure 3.13: Same as figure (3.7) for MW1 at $z=1.5$.

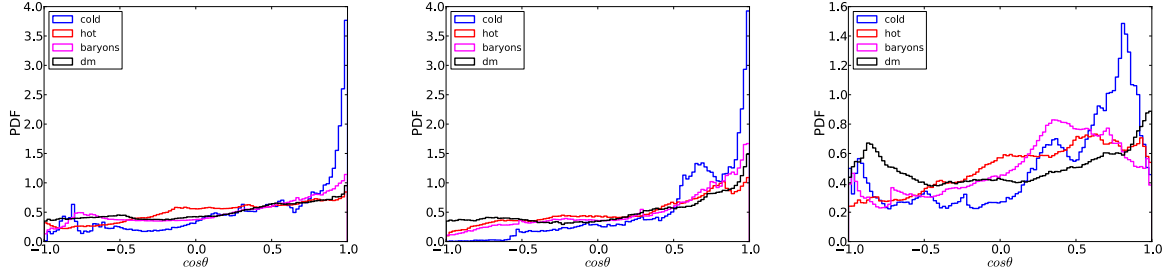


Figure 3.14: Distributions of $\hat{J} \cdot \hat{J}_{tot}$ within the halo for SFG1 at $z=3.17$ (Left), MW8 at $z=2.33$ (middle) and MW1 at $z=1.5$ (right). Shown are the distributions of the cosine of the angle between each particle or cell AM and the total AM of that component, showing the higher coherence of the cold gas compared to the other components having similar distributions. The median values for the cold gas, hot gas, baryons and DM for SFG1 are: 0.52, 0.23, 0.31, 0.23, for MW8: 0.69, 0.36, 0.48, 0.33 and for MW1: 0.42, 0.23, 0.28, 0.09.

3.3 Disc and halo AM alignments

In this section we look at AM in the direction of the disc spin axis, alignments between the disc and the outer halo region AM vectors and between the different component within the halo. In figure 3.15 we look at radial profiles of the spin parameter similar to the ones in figure 3.4 only using the AM in the direction of the disc spin axis instead of the total AM, thus seeing the radial evolution of the AM of the different components aligned with the disc spin axis. First, we see that as for the total spin parameter, also in this case, the cold dense gas dominates with the highest spin parameter or specific AM compared to the other components at all radii and all times. Second, we see that despite the fact that the cold gas as a whole has a very high spin parameter, in the direction of the disc it is lowered towards values much closer to the disc spin parameter assumed based on the DM spin parameter in semi-analytic models i.e. $\lambda \sim 0.05$. Finally, We see that unlike for the total spin parameter of each component, the spin parameter in the direction of the disc spin axis has a flatter profile starting from already outside the virial radius, and we don't see a drastic decrease in the spin parameter in the inner region as we saw previously, although there is some decrease in the two later snapshots. This hints towards the idea that the decrease we saw previously starting at the inner halo has to do with interaction of the disc or the disc region with the infalling material, as we will further explore in the next chapter. In figure 3.16 we show the alignment of the AM in shells at different radii with the disc spin axis for the cold gas. We focus on the cold gas for clarity since the other components turn out to have very similar profiles. The profile shows at the three snapshots, on average, a flat profile that starts to rise at $0.5R_v$ towards maximal alignment with the disc. The increased alignment starts roughly at the same region where we saw the decrease in the total spin parameter of the cold gas and the other components. Finally, in figure 3.17 we look at the alignment between the cold gas and the other components within the halo, as well as the alignment between the different components in the outer

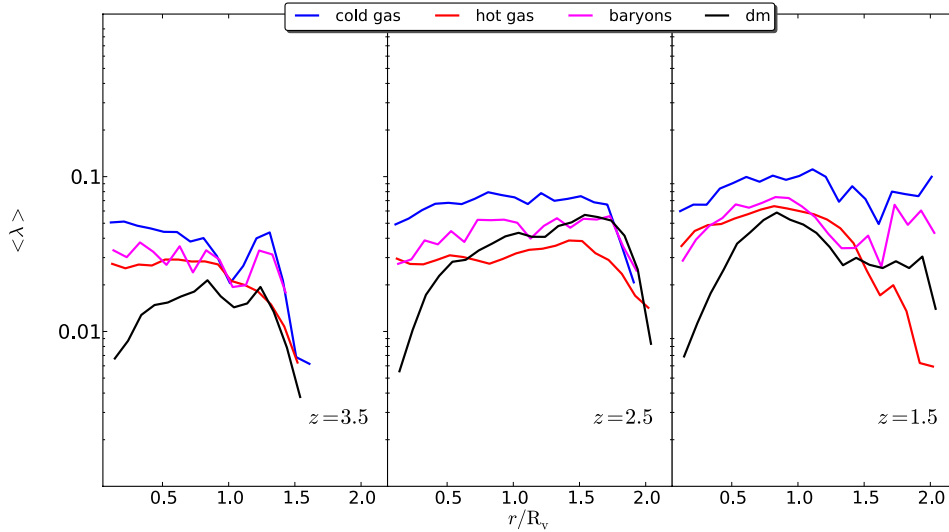


Figure 3.15: Spin parameter radial profiles, in the direction of the disc spin axis ($0.1R_v - 2R_v$) at 3 different redshift snapshots $z = 3.5, 2.5$ and 1.5 . Shown for each snapshot is the spin parameter of a given component (restricted to $V_r < 0$ in a thin shell of thickness $0.1R_v$ averaged over all halos. The errorbars were suppressed for clarity.

halo $> 0.1R_v$ and the disc spin axis. We see that the components are well aligned with each other. This fact in itself is not obvious, however within the framework of TTT considering that the direction of the torques acting on the different components are determined by the large scale environment this result is expected. The second plot of the alignment of the components within the halo and the disc is more surprising, since it shows not a strong alignment with a median of $\langle \cos \theta \rangle \sim 0.6$ for all components. This indicates that the disc can have quite a different behavior than the outer halo, and different than what one would expect from simple semi-analytic models, i.e. (Mo et al., 1998), in which the disc forms from the AM conserving collapse of the baryons, and thus the direction of the AM of the disc should be reflected by the AM of the DM or baryons in the halo, which it does, but relatively weakly on average.

3.4 Disc spin parameter and radius

In this section we look at the AM content of the disc and its implications on the disc radius. Specifically we test the validity of semi analytic models which follow TTT and the two mentioned assumptions, i.e. equal initial AM distributions of baryons and DM and conservation of AM during the baryonic collapse to model the disc radius. The galaxy radius was computed as described in (Ceverino et al., 2012), the radius is determined by using the cold ($T < 1.5 \times 10^4 K$) gas within a cylinder with z-axis coinciding with the

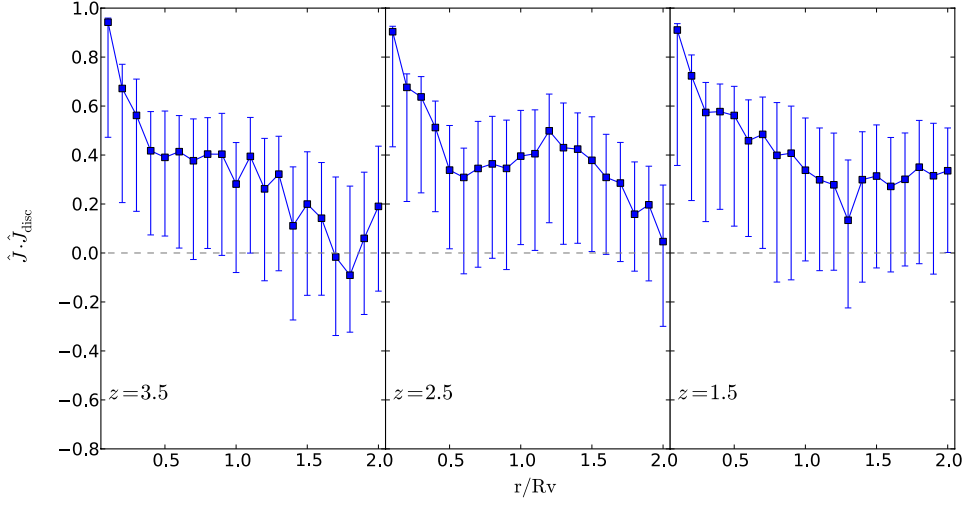


Figure 3.16: Radial profiles of $\hat{J} \cdot \hat{J}_{disc}$ in the range $(0.1R_v - 2R_v)$ at 3 different redshift snapshots $z = 3.5, 2.5$ and 1.5 . Shown for each snapshot is the median cosine of the angle between the AM vector of the shell (thickness $0.1R_v$) and the disc spin axis averaged over all halos at the appropriate snapshots. The profiles are for the cold gas component, the other components have similar profiles.

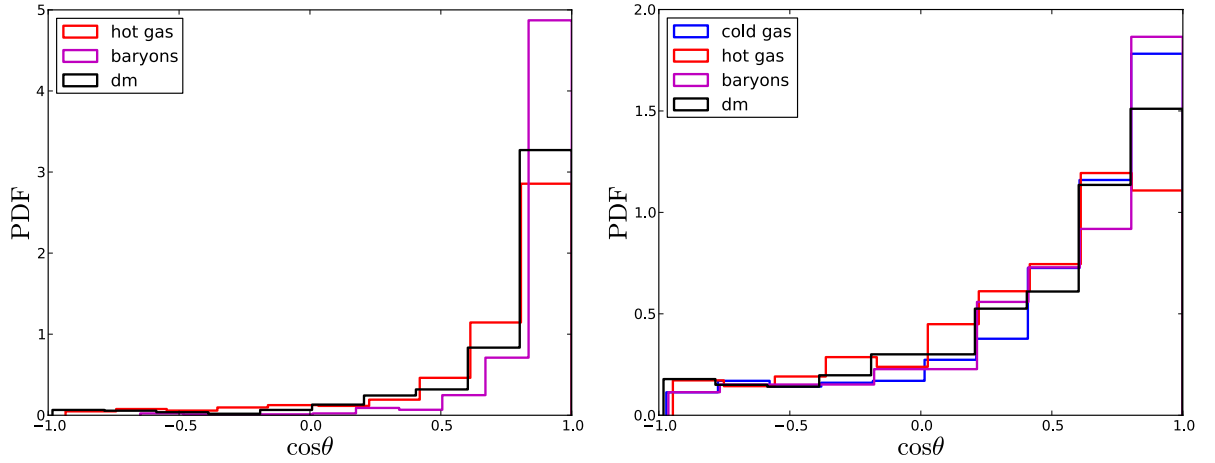


Figure 3.17: Distribution of the cosine of the angle between the cold gas and the other components AM vectors within the halo (Left), and between the components and the disc spin axis (Right). The median values for the alignments between the components and the cold gas are: 0.83, 0.95, 0.90 for the hot gas, baryons and DM, respectively. And for the disc and the different components: 0.7, 0.54, 0.67, 0.63 for the cold gas, hot gas baryons and DM, respectively.

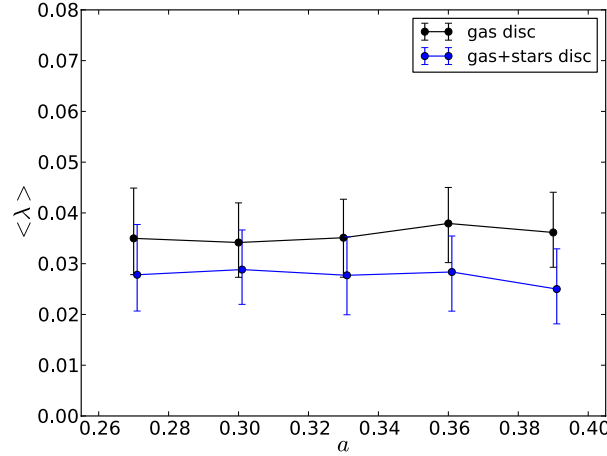


Figure 3.18: Disc spin parameter as a function of the expansion factor. Shown are the mean spin parameters of the gaseous (black) and gaseous+stellar (blue) disc for all halos at $a > 0.26$ satisfying the disc criteria. Each time bin contains three snapshots.

spin axis of the cold gas within it, and iteratively reducing the cylinder radius until it contains 85% of the gas mass within the large cylinder. The AM of the disc is composed of the AM of the gas and the stars. The gas AM is computed within the galaxy radius and height. The stellar component AM is computed within $2r_{gal}$ and $2h_{gal}$ but restricted to the disc (avoiding the bulge component) by imposing a kinematical criteria on the stars $j_z > 0.8j_{max}$, where j_z is the AM in the direction of the disc spin axis, and j_{max} is the maximum possible AM of the particle given its velocity and distance to the center. In addition, we restrict the analysis to galaxies satisfying $h_{gal}/r_{gal} < 0.5$ and we focus on $a > 0.26$ or $z < 0.3$ in order to ensure well defined discs. In figure 3.18 we show the evolution of the spin parameter of the gaseous disc and the gaseous+stellar disc. We see that as for the baryons and DM within the halo, the spin parameter has no evolution with time, with a constant $\langle \lambda_{gas} \rangle \sim 0.035$ and $\langle \lambda_{disc} \rangle \sim 0.028$. In figure 3.19 we show the distributions of the two spin parameters. We find the gaseous disc to be better fitted by a normal distribution with a mean $\langle \lambda \rangle = 0.036$. For the gas+stellar disc we fit to both a normal and log normal distributions, with the log normal (green) fit giving $\langle \lambda \rangle = 0.025$ and the normal distribution (red) fit gives $\langle \lambda \rangle = 0.028$. The missing high λ tail for the gaseous disc which result in the normal distribution rather than the log normal distribution can be a result of the fact that gas can contract to the center compared to the stars which can be pushed farther away from the center. The major importance of the AM of the disc is in determining its radius. In principle the disc specific AM can be written as follows,

$$j_d = f R_d V_d \quad (3.8)$$

Where R_d is the disc radius, V_d is some characteristic velocity and f is a numerical factor that depends on the specific disc model, specifically on its surface density distribution. A typical example is that of an exponential surface density $\Sigma(R) \propto e^{-R/R_d}$ which leads to

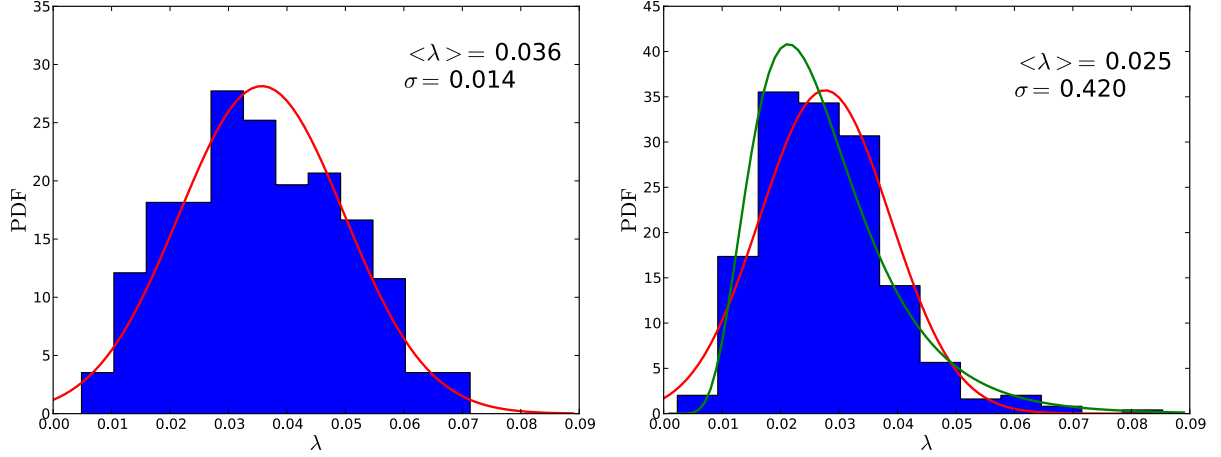


Figure 3.19: Spin parameter distributions for the gaseous (Left) and gaseous+stellar (Right) discs. Shown are the distribution of the two spin parameters fitted to a normal distribution (red) and log normal distribution (green) in the case of the gas+stellar disc.

$f = 2$. Using this we can get an expression for the disc radius involving both the disc related quantities and the virial related quantities. Starting from the expression for the dark matter spin parameter $\lambda_{DM} = \frac{j}{\sqrt{2}R_v V_v}$, where j is the specific AM of the DM halo, we multiply and divide by the disc specific AM and use (3.8) to get,

$$\lambda_{DM} = \frac{j}{\sqrt{2}R_v V_v} \frac{f R_d V_d}{j_d}. \quad (3.9)$$

The disc is known to have a constant rotation curve and we can write the constant velocity in terms of the virial velocity $V_d = v V_v$, where v is a factor of order unity. We plug this into (3.9) and rearrange to get an expression for the disc radius,

$$R_d = \sqrt{2}(fv)^{-1} \left(\frac{j_d}{j} \right) \lambda_{DM} R_v \quad (3.10)$$

Therefore, there is a simple relation between the disc radius and the virial radius depending on the halo spin parameter. The important term in this relation is the ratio of the specific AM of the disc and the halo $R_{dm} = j_d/j$. This factor contains the information regarding the actual processes involved in the formation of the disc, i.e. which material formed it and with what AM. However, j_d can be affected also by local processes within the disc, primarily feedback which can specifically remove low AM material from the disc. The common assumption made in semi-analytic models is setting $R_{dm} = 1$, which is motivated by the ideas of equal initial AM distributions for the DM and the baryons, and conservation of AM during the collapse. In figure 3.20 we show this ratio measured from the simulations as a function of time for both the gaseous and gas+stellar discs. We see that on average $R_{dm} \sim 0.95$ implying, the assumption of $R_{dm} = 1$ is a good assumption for the gaseous disc

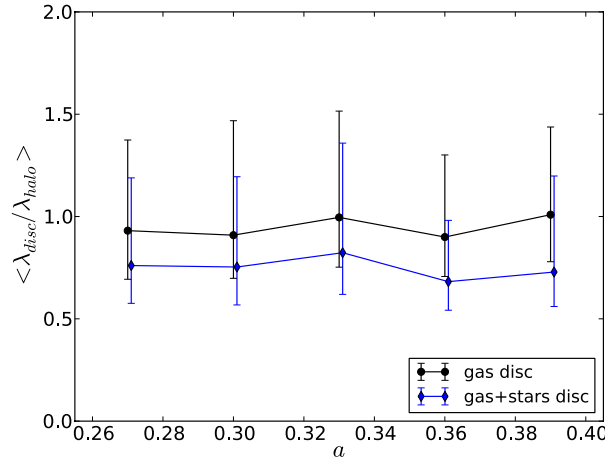


Figure 3.20: Spin parameter ratio between the disc and the halo. Shown are the mean values of $R_{dm} = \lambda_{disc(gas)}/\lambda_{dm}$ (black) and $\lambda_{disc(gas+stars)}/\lambda_{dm}$ (blue) as a function of a , stacked over all halos. The ratio is constant with time and around 0.95 for the gaseous disc indicating $j_d \sim j_{dm}$.

at all times, however there is significant scatter in the range of 20 – 40% which translates to a similar deviation in the expression for the galaxy radius, when assuming $R_{dm} = 1$. The gas+stellar disc has $R_{dm} \sim 0.75$. We note that using a higher kinematical criteria for the stellar disc (i.e., $j > 0.9j_{max}$) will lead to higher ratios. Comparing the spin parameters of the disc and the cold gas components gives values of $j_{d(gas)}/j_{cold} \sim 0.4$ for the gaseous and $j_{d(gas+stellar)}/j_{dm} \sim 0.33$ for the stellar disc, indicating that the specific AM content of the disc is quite small compared to the available cold gas which forms it. Alternatively, if we look at the ratio of the median spin parameters obtained from the fitted distribution ($\lambda_{disc}/\lambda_{dm}$) we get $\langle R_{dm} \rangle = 0.86$ for the gaseous disc and $R_{dm} = 0.6$ for the gas+stellar disc. The value for the gas+stellar disc is the same as obtained in (Dutton and van den Bosch, 2012) using constraints from observations on galaxy-dark matter connection, they find the same ratio of 0.6. These values which are less than one, indicate $j_d < j_{dm}$ however this doesn't necessarily imply lack of conservation of AM. This can be interpreted either that indeed baryons lost a certain amount of their initial AM or that the baryons that actually formed the galaxy have a lower AM than the baryons as a whole, or it could be a combination of the two. Finally, feedback due to star formation can change the distribution of AM within the disc and the disc AM as a whole, primarily removing low AM material which is more susceptible to such processes, however this will not explain the lower values of j_d compared to j_{dm} . Observations of disc galaxies scale lengths vs. rotational velocity (Courteau, 1997), show that the predicted scale lengths from the cosmological models are too large, and require some AM loose from the gas (retaining 70% of its AM), as one way to reconcile the model with the observations. Finally, we use two sets of newer simulations compared to the ones used throughout this work, called generation (gen) 2 and 3, which are identical to each other except for the

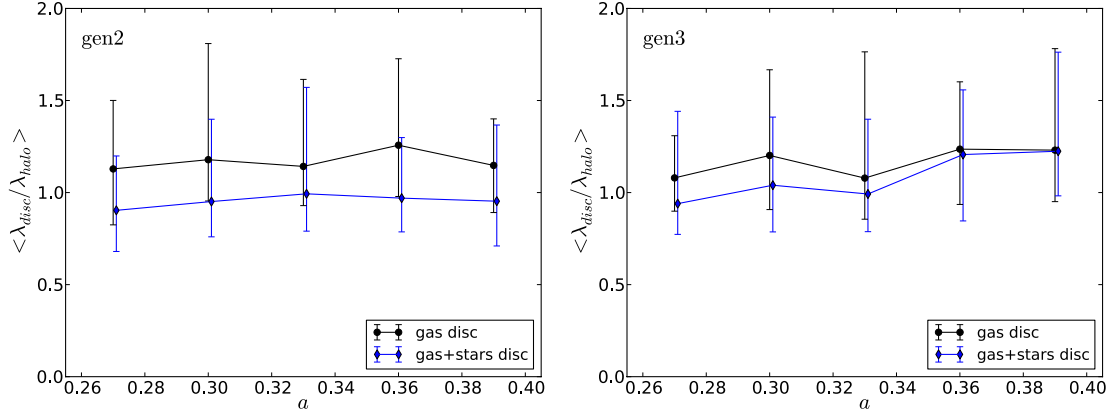


Figure 3.21: Spin parameter ratio between the disc and the halo. Shown are the mean value of $\lambda_{disc(gas)}/\lambda_{dm}$ (black) and $\lambda_{disc(gas+stars)}/\lambda_{dm}$ (blue) as a function of the expansion factor, stacked over all halos in gen. 2 (Left) and gen. 3 (Right).

stronger feedback in gen. 3 and the overall higher resolution compared to gen. 1, although they have smaller halo masses compared to gen. 1, not exceeding $10^{12} M_{\odot}$ at all times. We show the same ratios of specific AM of the disc and DM in figure 3.21. We see that both ratios are higher than obtained for gen. 1, and also that on average the gaseous disc has a higher value than 1 indicating $j_d > j$ which is what we expected for a stronger feedback. In these simulations the gaseous+stellar disc is closer to 1, and even exceeds it at later times in gen. 3. Comparing the disc spin parameter to the cold gas component gives values around ~ 0.5 .

Chapter 4

Torques and AM exchange in the inner halo

4.1 The 'Messy Region'

In the previous two chapters we saw a number of results which indicate the presence of a region in the inner halo where various processes occur that might have significant affect on the AM that reaches the disc. The notion of such a region was already introduced in (Danovich et al., 2012) and was termed the 'Messy Region', and also in (Kimm et al., 2011) where the gas specific AM is seen to diminish in the inner halo region. These results include the limited penetration of the stream plane down to $\sim 0.5R_v$, the decrease in the spin parameter of the cold gas especially starting at $\sim 0.4R_v$ from the typical value of $\lambda \sim 0.1$ to $\lambda \sim 0.04$ in the vicinity of the disc, the increased alignment of the AM of the different components with the disc starting at the same region and the general weak alignment between the disc spin axis and the outer halo. In this chapter we study this region more closely and test the claim of significant AM exchange in this region. In figure 4.1 we show density projections of the $0.5R_v$ region for four galaxies at different times showing visually the features of this region as a relatively high density region with irregular motion and disruption of the infalling gas. The region is seen to be at the interface between the accreting cold streams falling undisturbed in the outer halo and the more disturbed disc region. In the four examples we see 2-4 streams reaching this region either radial or have some impact parameter as seen in the bottom row of that figure. We see that typically the radius of the messy region is visually determined by the cold stream with the largest impact parameter, such that for the top left the messy region is closer to $0.1R_v$ while for the other cases it is around $0.3R_v$. We remember from figure 3.6 that the mean impact parameter for the cold gas within the halo was also around $0.3R_v$ supporting this claim. The fact that we see this at different redshifts and different virial radii, implies that this region size scales with the virial radius and therefore increases with time, as does the impact parameter of the cold gas which we saw in the same figure.

Motivated by the visual inspection, we now focus on a number of quantities of interest

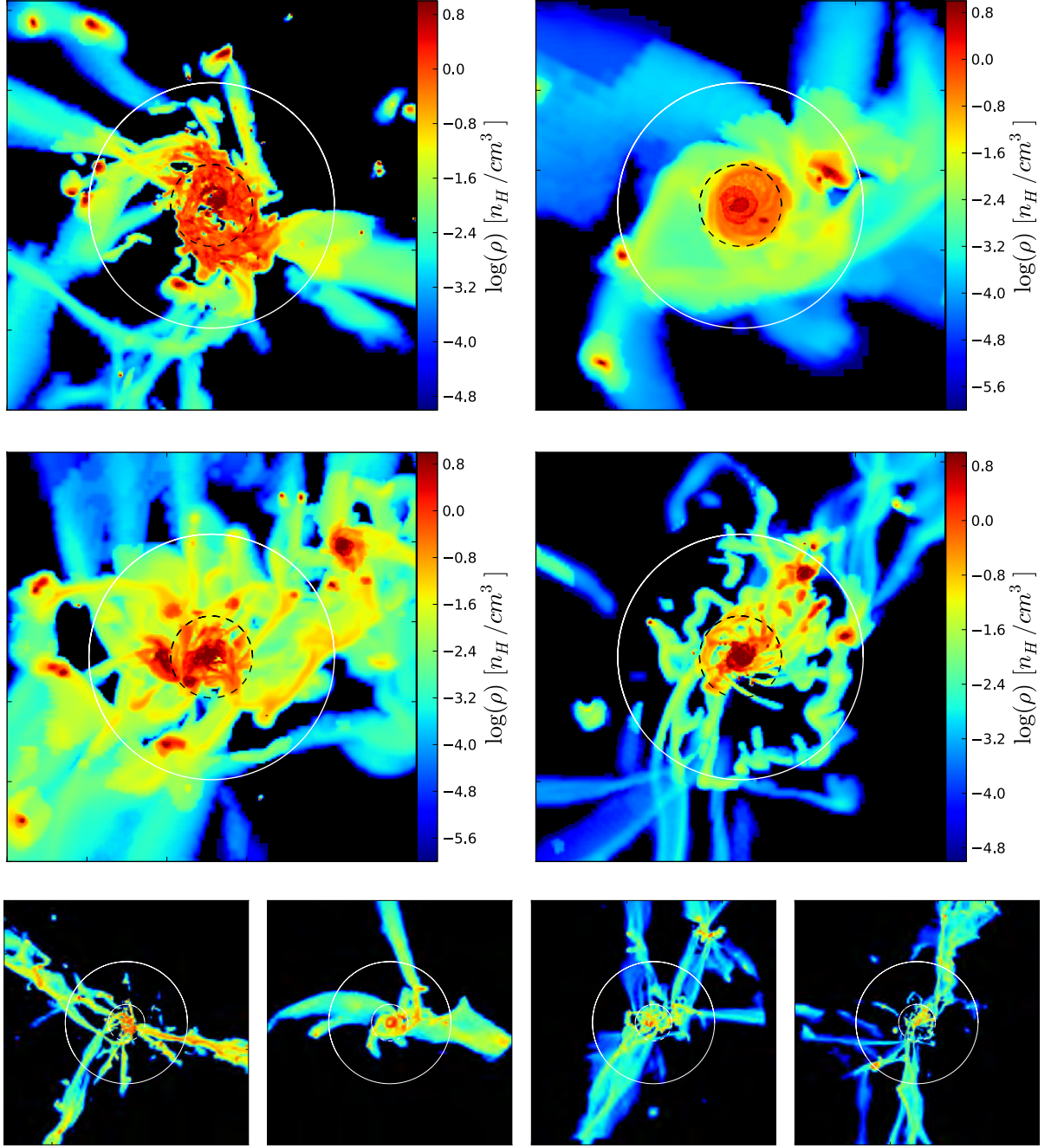


Figure 4.1: Density projections of the cold dense gas in the $< 0.5R_v$ region. The projections are face on in the direction of the disc spin axis and of thickness $1R_v$. The galaxies are: (Top left) SFG1 at $z=3.17$ with $R_v = 85.75\text{kpc}$ and $M_v = 1.27 \times 10^{12}M_\odot$, (Top right) MW8 at $z=2.33$ with $R_v = 60.75\text{kpc}$ and $M_v = 2.34 \times 10^{11}M_\odot$, (Bottom Left) , MW3 at $z=1.94$ with $R_v = 104.0\text{kpc}$ and $M_v = 6.92 \times 10^{11}M_\odot$ (Bottom right), MW1 at $z=1.63$ with $R_v = 129.5\text{kpc}$ and $M_v = 1.16 \times 10^{12}M_\odot$. The white circle has a radius of $0.3R_v$ and the inner dashed black circle marks the $0.1R_v$ disc region. The bottom row shows the same galaxies from left to right, top to bottom, on the virial scale, box size of $4R_v$, with the virial radius marked by white circle, and $0.3R_v$ marked by the dashed circle. Showing the connection of the streams to the messy region.

for understanding this region. In figure 4.2 we show 2D histograms for the same galaxies shown above, as a function of the radius. In all plots the color is in log scale and codes the mass in each pixel, and the red line is the mass weighted mean. The first quantity demonstrates the type of motion of the gas in this region by showing the ratio of the tangential and radial velocities V_θ/V_r . We see that other than substructures at large radii which can have high V_θ , the ratio there is mostly below 1, until we reach the inner $0.5R_v$ where the ratio increases up to the disc itself. The second quantity is the impact parameter of the cold gas, separated to positive or negative depending on the orientation of each cell's AM with respect to the disc. In this case the red line is the mass weighted mean of the absolute value of the impact parameter. We see in the four cases a generally flat mean profile starting at around the virial radius (due to the cold streams) down to $\sim 0.3R_v$ where we see a dark patch at a linearly decreasing impact parameter, indicating a large amount of mass in rotational motion. In three of the four cases, most of the mass in this region is co-rotating with the disc, and in one case there is comparable mass also counter-rotating. This raises the possibility of counter rotating stars in the disc, as was also found in (Algorry et al., 2013) as well as in a number of observations. We measure the mass fraction relative to the total stellar mass of the stellar disc in rotating and counter rotating stars, defined using the same kinematical criteria (with an opposite sign) for the four examples and find for SFG1 25%, for MW8 8%, for MW3 4%, MW1 49%. Some of these values are non-negligible fractions and have no direct explanation within standard models of galaxy formation involving spherical collapse. However, within the framework of filamentary accretion and the previous results this is more naturally explained as was again pointed out in (Algorry et al., 2013), this component can result from the accretion of gas through a cold stream with negative AM compared to the disc. The third quantity is the total specific AM of the cold and dense gas. The blue line in these histograms marks the maximum specific AM possible for a particle in a Keplerian orbit at a given radius given the total interior mass (this assumes a spherical potential), $j_{max} = (GM(< r)r)^{0.5} = vr$, i.e. a circular motion. We see that the mean is typically below the maximum for a Keplerian orbit, however there is gas also with a higher value. We see that the drop at the inner region where there is a dark patch starting at $0.2 - 0.3R_v$, follows closely this maximum value (with some mass below and above), indicating a mostly rotational motion there. The final quantity we show is the alignment of the cold gas AM with the disc spin axis, where we see increased alignment in the form of dark patches rising towards higher values in the inner region, as well as disappearance of negatively aligned gas when approaching the inner region. Filamentary structures are seen in these histograms as elongated horizontal strips. The notion of an extended rotating cold gas much beyond the disc region was already described in (Stewart et al., 2013) and was later observed by (Bouche et al., 2013) which find evidence for cold mode accretion in the form of a cold gas component rotating around a central galaxy at $z = 2.3$ and estimated virial mass of $10^{11}M_\odot$, which is similar to our MW8 galaxy shown in figure 4.1. The rotating cold gas is found at $\sim 1/3$ of the virial radius, which exactly corresponds as in our case to the messy region.

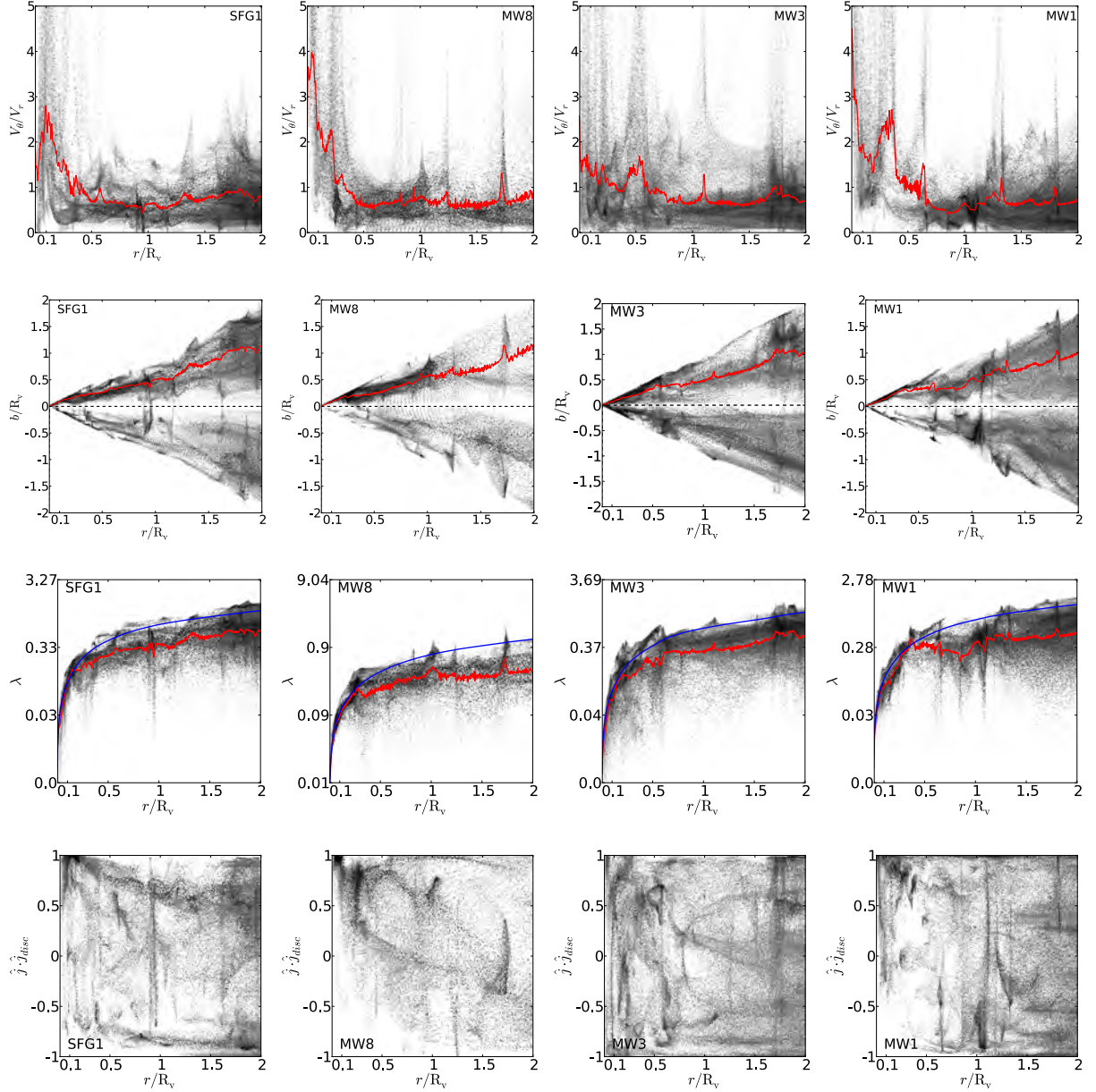


Figure 4.2: 2D histograms for the galaxies shown before of the following parameters for the cold gas as a function of radius (from top to bottom): V_θ/V_r , b/R_v -impact parameter, $\log \lambda$ - spin parameter (axis shows λ) and $\hat{J} \cdot \hat{J}_{disc}$. The color corresponds to the log of the mass in each pixel and the red line is the mass weighted mean. These demonstrate the transition from the outer halo to the messy region being characterized by mostly rotational motion, radius defined by the impact parameter of infalling gas, specific AM mostly limited by a Keplerian orbit (blue curve), and increased alignment with the disc spin axis.

4.2 Torques and AM exchange

In order to examine the importance of torques on the accreting gas, we first develop the general expression for the evolution of AM of a fluid in the presence of gravity. The angular momentum per unit volume of a fluid in a given position is $l_i = \epsilon_{ijk}\rho x_j v_k$, its rate of change is therefore,

$$\frac{\partial l_i}{\partial t} = \epsilon_{ijk} x_j \frac{\partial \rho v_k}{\partial t} = \epsilon_{ijk} x_j \left(v_k \frac{\partial \rho}{\partial t} + \rho \frac{\partial v_k}{\partial t} \right). \quad (4.1)$$

Using the continuity equation and Euler's equation of motion,

$$\frac{\partial \rho}{\partial t} + \frac{\partial \rho v_k}{\partial x_k} = 0 \quad (4.2)$$

$$\frac{\partial v_i}{\partial t} + v_k \frac{\partial v_i}{\partial x_k} = -\frac{1}{\rho} \frac{\partial P}{\partial x_i} - \frac{\partial \phi}{\partial x_i}, \quad (4.3)$$

inserting them in the expression for the rate of change of the angular momentum gives,

$$\frac{\partial l_i}{\partial t} = -\epsilon_{ijk} x_j \left(v_k \frac{\partial \rho v_m}{\partial x_m} + \rho v_m \frac{\partial v_k}{\partial x_m} + \frac{\partial P}{\partial x_k} + \rho \frac{\partial \phi}{\partial x_k} \right). \quad (4.4)$$

We open up the first term, and insert ρ inside the derivative in the second term, in order to get an advection term:

$$\frac{\partial l_i}{\partial t} = -\epsilon_{ijk} x_j \left(v_k v_m \frac{\partial \rho}{\partial x_m} + \rho v_k \frac{\partial v_m}{\partial x_m} + v_m \frac{\partial \rho v_k}{\partial x_m} - v_m v_k \frac{\partial \rho}{\partial x_m} + \frac{\partial P}{\partial x_k} + \rho \frac{\partial \phi}{\partial x_k} \right) \quad (4.5)$$

$$\frac{\partial l_i}{\partial t} = -\epsilon_{ijk} x_j \left(v_m \frac{\partial \rho v_k}{\partial x_m} + \rho v_k \frac{\partial v_m}{\partial x_m} + \frac{\partial P}{\partial x_k} + \rho \frac{\partial \phi}{\partial x_k} \right). \quad (4.6)$$

The first term is an advection term which we can move to the left hand side and write it using the Lagrangian derivative, we finally get:

$$\frac{d\vec{l}}{dt} = -\epsilon_{ijk} x_j \left(\rho v_k \frac{\partial v_m}{\partial x_m} + \frac{\partial P}{\partial x_k} + \rho \frac{\partial \phi}{\partial x_k} \right). \quad (4.7)$$

The three terms on the right hand side that determine the rate of change of the angular momentum in the fluid are: $-\vec{l} \nabla \cdot \vec{v}$ which is a result of the strain and is proportional to the divergence of the velocity field and the angular momentum, and therefore can only change the magnitude. The strain term results from viscosity which couples the off-diagonal elements in the stress tensor to the Hydro equations, however in the simulation we have only a small numerical viscosity and therefore this term is less significant compared to the other two as we indeed checked. The second term is $-\rho \vec{r} \times \nabla P$ which is a torque resulting from a gradient in the pressure. The third term is $-\rho \vec{r} \times \nabla \phi$ which is the torque resulting from the gravitational forces on the fluid. The torques calculation which requires the calculation of the gravitational forces at each point, was done using a tree-code algorithm.

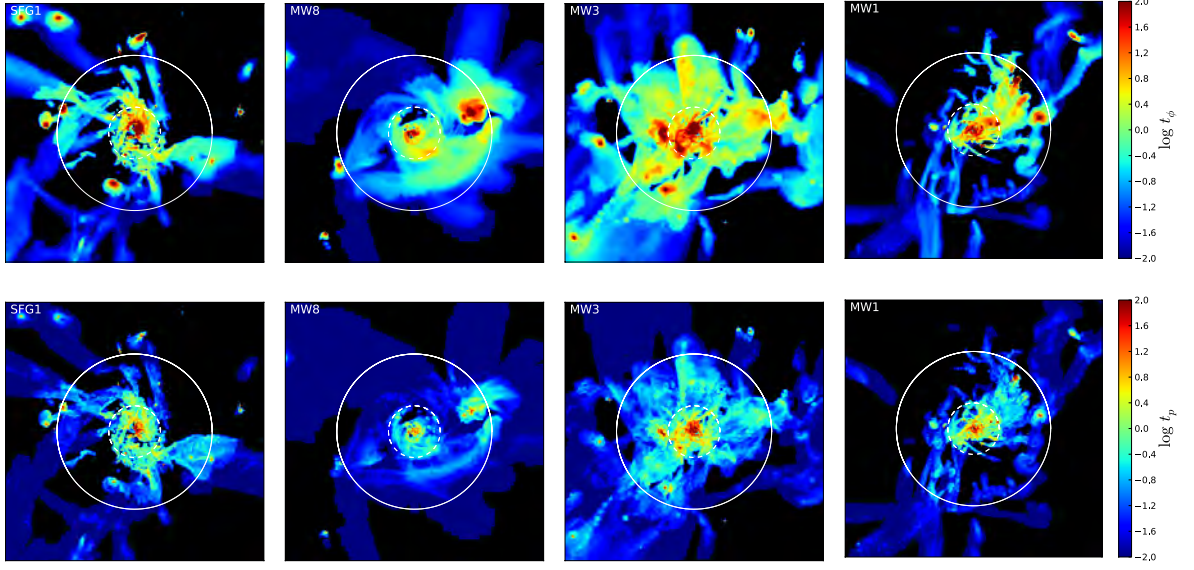


Figure 4.3: Projections of the gravitational (Top) and pressure (Bottom) torque parameters for the four galaxies in a box of size $0.5R_v$ and thickness $0.6R_v$. The outer circle marks $0.3R_v$ and the inner dashed circle marks $0.1R_v$. The projections are in the face on direction of the disc.

The opening angle used is $\theta = 0.8$, which determines the accuracy of the force calculation, and a softening length of 4 grid cells. The derivatives were calculated on a uniform grid extracted from the AMR grid using a tricubic spline interpolation scheme.

We define the following dimensionless parameters measuring the ability of the two torques to change the AM of a given gas cell:

$$t_\phi = t_c |\mathbf{r} \times \rho \nabla \phi| / |l|, \quad t_p = t_c |\mathbf{r} \times \nabla p| / |l| \quad (4.8)$$

Where t_ϕ is the gravity torque parameter and t_p is the pressure torque parameter. t_c is a time scale which is needed to make the parameters dimensionless. We choose this time scale to be $t_c = 0.2R_v/V_v$ which is the dynamical time in the approximate messy region where the cold gas is in orbit. For our examples, this value ranges from 70 to 140 Myr. We begin by showing projections of the two parameters in figure 4.3. We see in these examples that the torques are the strongest in the inner $0.3R_v$ region, and the gravitational torque is more dominant than the pressure torque, acting also along the filaments. In principle, the pressure torque is expected to act in the interface between hot and cold gas in which a pressure gradient occurs.

Next we turn to the defined parameters and calculate them for the cold gas component. In figure 4.4 we show 2D histograms of these parameters as a function of radius. Looking at the mass weighted mean traced by the red line, we see an increased slope and more mass at higher values in the $< 0.5R_v$ region for both torques. We see that the gravitational torques profile is strongly affected by sub structures, where the torque is a result of the gravitational force on the gas from the satellite center, such that the total torque is zero, despite the

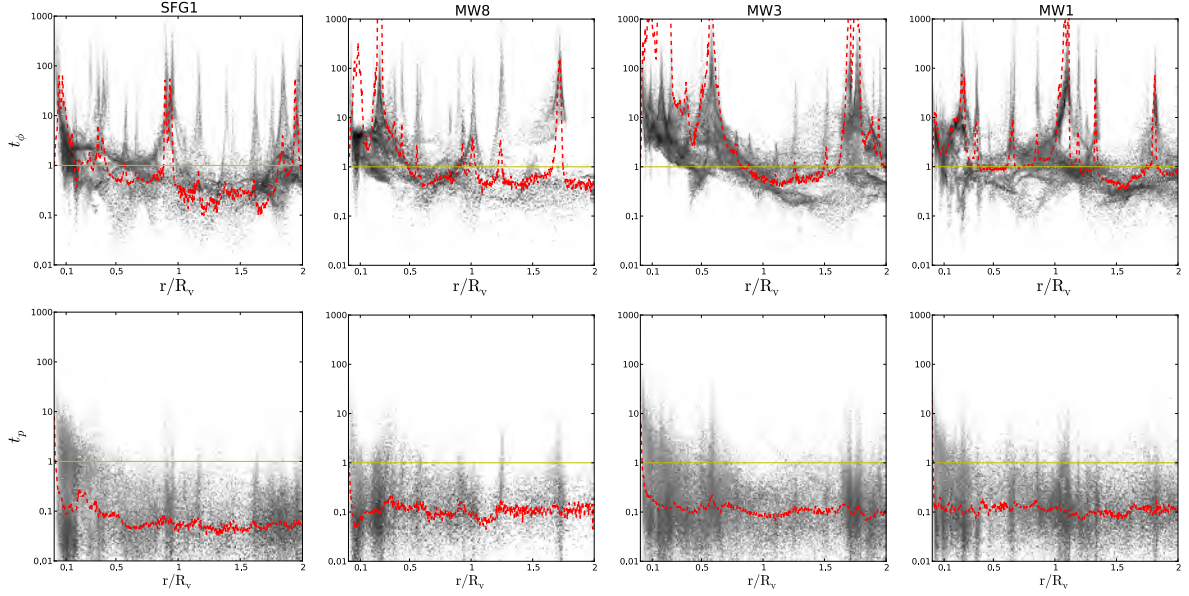


Figure 4.4: 2D histograms of the torque parameters t_ϕ, t_p (rows) for the four galaxies from above (columns) as a function of the radius. The color corresponds to the log of the mass in each pixel and the red line is the mass weighted mean. Showing the relative dominance of the gravitational torques over the pressure, and their increased importance in the inner regions.

high peak. The meaning of the values is that if the torques act for t_c/t_ϕ or t_c/t_p years it can change the angular momentum by a 100%. We note that the actual time scale in which the torques operate can be different in the different regions, and especially this time is the largest in the messy region, since there the gas is in orbit, compared to the outer halo where the cold gas basically free falls to the center. This makes the torques in the inner region even more significant. The orbital period for a circular motion at the messy region radius is simply $T_{orb} = 2\pi t_c$, the typical values of the orbital periods for the examples are between 450 and 880 Myr. From the histograms the typical values for the torques in the inner region are $t_\phi \sim 5$ and $t_p \sim 0.5$. This means that the gravitational torques can change the AM by an order of unity in 1/5 of the orbital time, while the pressure torques in 2 orbital times. Next we want to look more specifically at the actual effect of the torques on the AM vector of the cold gas. Specifically, do the torques act to reduce the amplitude. In figure 4.5 we first show profiles of the spin parameter and alignment with the disc for the four galaxies, in order to see what we should expect from the torques. In three of the cases we see the familiar features stressed before, of a rather flat profile throughout until the inner region where the spin parameter drops steadily, and at the same time an increased alignment with the disc. In the first example, we don't see a clear decline in the inner region, only between the last two points at $0.2R_v$ and at $0.5R_v$. In the first two examples cold gas is well aligned with the disc throughout the halo. The other two examples show a steady decline starting at $\sim 0.4R_v$ with increased alignment, despite a weak one for the third example. It is useful

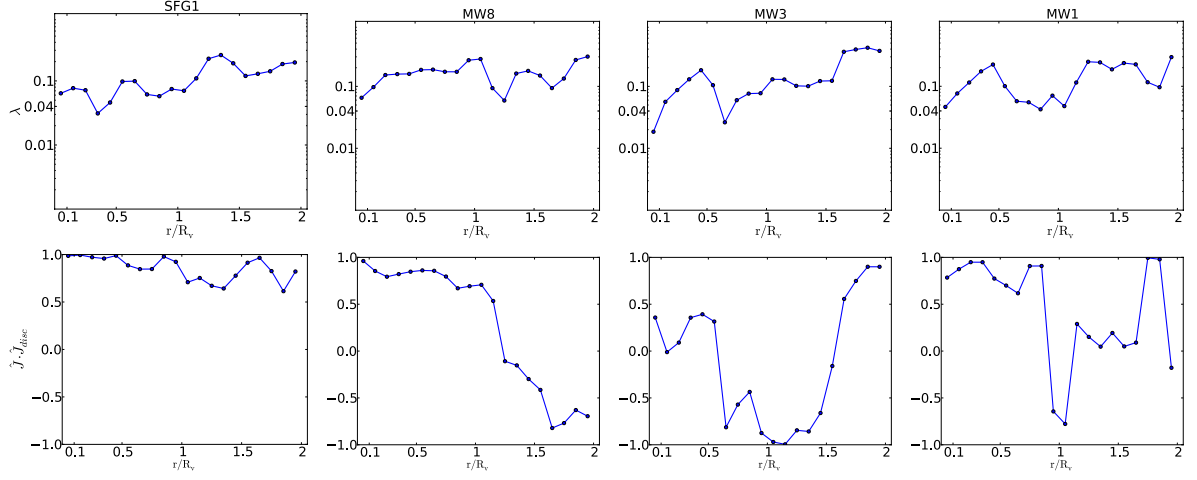


Figure 4.5: Radial profiles of the spin parameter of the cold gas (Top) and AM alignment with the disc spin axis (Bottom) for the four galaxies between $0.05 - 1.95R_v$ using thin shells of radius $0.1R_v$.

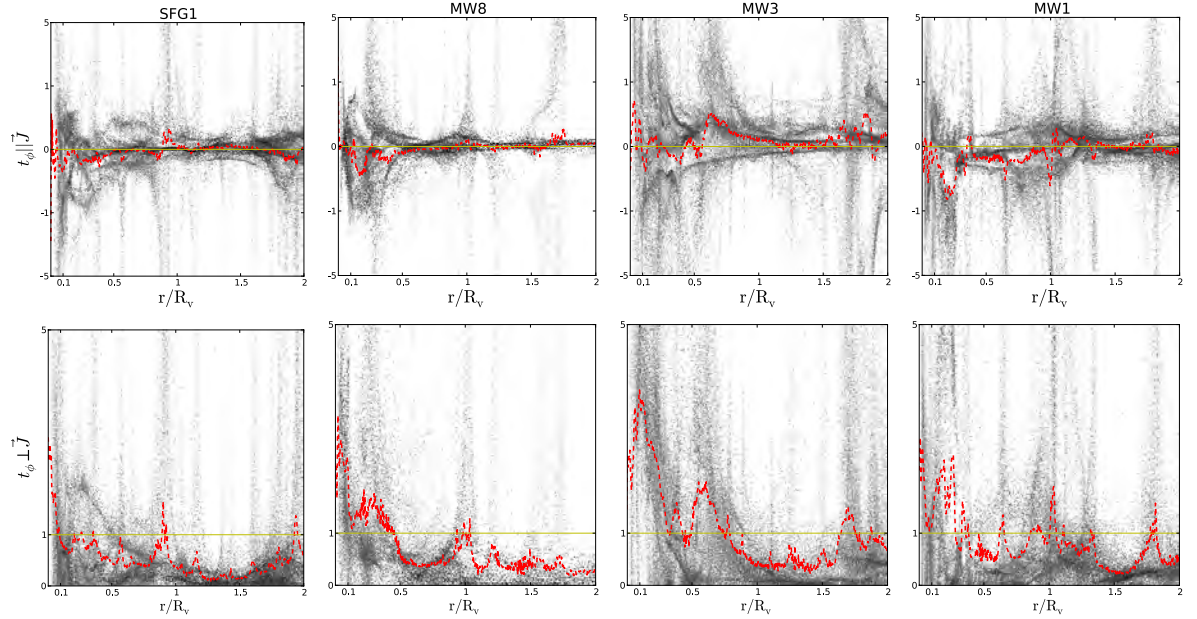


Figure 4.6: Radial profiles for the four galaxies (columns) of: (Top) the gravity torque parameter in the direction of the AM of each gas cell, i.e. the effect of the torque only on the amplitude of the AM. (Bottom) The gravity torque parameter in the direction perpendicular to the AM vector of each cold gas cell.

to quote also the value of the spin parameter of the disc in these cases, we quote both the gas and gas+stellar values. For SFG1: $\lambda_{gas} = 0.049$, $\lambda_{gas+stellar} = 0.052$. For MW8: $\lambda_{gas} = 0.04$, $\lambda_{gas+stellar} = 0.03$. For MW3: $\lambda_{gas} = 0.014$, $\lambda_{gas+stellar} = 0.016$. For MW1:

$\lambda_{gas} = 0.021$, $\lambda_{gas+stellar} = 0.018$. In some of the cases we see from the profiles that the value of the cold gas spin parameter is higher than these values, this could be either due to the fact that the disc contains material with smaller specific AM accreted earlier, or that not all of the cold gas ends up in the disc, at least not at this snapshot. In figure 4.6 we show 2D histograms of the gravitational torque parameter (since it is the dominant one) restricted to the component acting in parallel to the AM of each gas cell (increasing or reducing the AM amplitude). In three of the cases corresponding to the cases where a drop in the spin parameter was seen in the profiles, we see from the mean profile traced by the red line, that in the corresponding region, there is a negative overall contribution from the gravitational torques. We see that the profile is flat throughout composed of the contribution of the satellites gas as explained before, which cancel out. Another feature is that of horizontal lines which bend at the inner region, these are most likely filaments being increasingly torqued at the inner region. This is especially seen for MW3, where a filament is increasingly torqued towards lower AM values. The fact that in the inner region there is no exact cancellation, means that there are actual torques on the gas which preferentially reduce the AM amplitude. The way to interpret the values is by noting that $1/(2\pi x)$ where x is the value of the torque parameter, will give the number of orbits in the messy region before the AM changes by order unity. We see that it is typically some fraction of a full orbit, meaning that the cold gas doesn't complete a full orbit in most of the cases, but is brought to lower radii after some fraction of the orbit, around ~ 0.5 , as seen in the projections at the beginning of the chapter. In the second row we show the perpendicular component of the gravitational torque relative to the AM of the cold gas cells. We see that especially in the inner region, the perpendicular component becomes strong, being able to significantly change the direction of the AM, which matches the corresponding plots of the alignment with the disc. In the first example, since the cold gas is already aligned with the disc at all radii, the parameter remains below 1 throughout, only in the very center it becomes higher. While for the other examples, where we see a sharp alignment with the disc, there is a corresponding peak in the perpendicular component of the torque. We conclude that our results show that the gravitational torques acting in the inner region are capable of reducing the AM amplitude of the cold gas, as suggested by the spin parameter profiles, as well as reorient the AM in the direction of the disc.

Chapter 5

Summary and discussion

5.1 Summary

We summarize the main results of the last 3 chapters and then provide a general summary.

- **Cold streams and pancakes:** Our analysis of the cold streams in the cosmic web has revealed a number of non trivial properties characterizing the cold streams in massive dark matter halos at high redshifts ($z = 4 - 1.5$). There are typically three major streams directed towards the massive nodes of the cosmic web. These three streams tend to lie in a plane containing the galaxy center, with the plane being well aligned with the minor axis of the inertia tensor of the mass distribution within $2R_v$. The stream plane typically consists of additional low entropy gas with lower influx densities reminiscent of the initial one dimensional collapse resulting in a pancake structure which extends down to $\sim 0.4R_v$ where the ambient density becomes comparable and out to $\sim 5R_v$ where a complex network of filaments and sheets takes over. The three streams typically contain one dominant stream in terms of mass ($\sim 70\%$) and AM ($\sim 60\%$), and one stream that is most aligned with the disc. These features are non trivial statements about the nature of the cosmic web. The asymmetrical nature of the structure distribution near the massive dark matter halos or the nodes of the cosmic web, i.e. the presence of filaments and sheets, is described already by the Zel'dovich approximation which assigns the eigenvalues of the deformation tensor a specific morphology (filament, sheet, void and node), however this asymmetric distribution is already present in the Gaussian random field which describes the primordial density fluctuations, as shown by (Doroshkevich, 1970) obtaining the distribution of the eigenvalues of the local deformation tensor, showing that a perfectly spherical collapse has zero probability. As described, the presence of a filament requires a simultaneous coherence in two eigenvalues $(+,+,-)$ as a function of the distance from the node, whereas a sheet-like structure requires the coherence of only one eigenvalue $(+,-,-)$, which implies that is more likely to have filaments in extended sheets, since one of the eigenvalues is already coherent with distance in the case of sheets. In the vicinity of high overdensity peaks (the origin of the massive

dark matter halos) this coherence length is expected to be even greater, since the variance in the mean value of the eigenvalues at a distance r from the node is limited by the general variance over space (Dekel, 1981; Bardeen et al., 1986). The result of three major filaments or a minimum number of filaments, can be understood from the continuity of the eigenvectors of the deformation tensor within the smoothing length of the fluctuation field. Where the notion of a smoothing length is required in order to be able to speak about such objects as filaments percolating below a given overdensity smoothed on some scale. When the filaments reach the smoothing scale around the node, the eigenvalues and eigenvectors must converge to one set of values required from continuity, this will lead to a bifurcation point at which for example two filaments with a given opening angle between them will smoothly merge into a third filament which enters from the other side of the node. This then also supports the streams co-planarity as this picture implies a transition from 1D (the eigenvector in the direction of the merged filaments within the smoothed scale) to 2D beyond the bifurcation point, and eventually to 3D at more bifurcation points near other nodes. Finally, we note that the minimal average number of filaments per node is three, since using two filaments per node, one cannot construct even a 2D web. The partitioning of space originating from three filaments per node is that of a hexagonal grid or a honeycomb (in contrast to a cubical grid with four filaments per node). In this configuration the volume of the empty spaces or voids is maximal. The dynamics of the components of the cosmic web implies an expansion of the voids as we saw from the Zel'dovich approximation, making the voids more spherical by the gravitational forces, implying that the cosmic web favors or has a tendency towards a hexagonal grid configuration compared to a cubical for example.

- **AM content and transport in DM halos:** By studying the AM properties of the different components building up a dark matter halo we find that the cold gas has a significantly higher specific AM compared to all baryons, the hot gas and the dark matter components. This is true for the material within the halo, the material accreting into the halo and the component aligned with the disc spin axis. The spin parameter of the different components within the halo is well fitted by a log normal distribution. The spin parameters of the DM and baryons within the halo are relatively independent of mass and redshift at $\lambda \sim 0.042$, whereas the cold gas spin parameter has an increasing evolution with time with a mean $\lambda_{cold} \sim 0.1$. The AM of the accreting material as well as the total AM of the halo for the different components grows with time roughly with the growth of the virial quantities. The cold gas has a relatively smaller impact parameter but high velocities leading to comparable specific AM of individual gas and DM particles. The higher total specific AM of the cold gas compared to the other components is attributed to a higher coherence in the AM vectors addition, resulting from its spatial distribution along narrow filaments, compared to a more incoherent AM addition in the other components, resulting from mixing with old material with lower AM. We find that the disc spin parameter has no evolution with time and is comparable to that of the dark matter component at

~ 0.036 (fitted to a Gaussian) for the gaseous component with a scatter of $20 - 40\%$, but is about 60% compared to the DM spin parameter for the gas+stellar disc, with $\lambda \sim 0.025$. Higher resolution simulations and with stronger feedback show a tendency towards higher disc spin parameter even compared to the dark matter for the gaseous component and a ratio of $\lambda_{disc}/\lambda_{dm} \sim 1$ for the gas+stellar disc, implying similar specific AM of the disc and the halo in accord with semi-analytic models of the disc.

- **AM exchange in the inner halo:** We find the presence of a region connecting the outer halo and the disc at $\sim 0.4R_v$ termed the 'Messy Region' which we find is characterized by the presence of high density cold gas in mostly rotational motion about the disc region limited by a Keplerian orbit at this radius. The extent of this region is found to be determined by the largest impact parameter of the cold streams. As such, this region scales with the growth of the impact parameter of the cold gas which scales with the virial radius. We find that mostly gravitational torques can affect significantly the AM of the cold gas in the messy region. The source of the torques is not clear from our results. One possible source is the disc. Within the picture of the inner disc and outer extended and tilted disc, one can understand the source of the torques as originating from the disc and acting on the outer disc if the two are not aligned. The disc gravitational potential is axisymmetric (for an axisymmetric disc) implying that the only torque component possible is the azimuthal direction (for a disc at the origin). This will tend to align the outer disc with the inner disc, by applying a torque perpendicular to the AM direction of the outer disc. In order for the gravitational torque to act to reduce the AM amplitude, the azimuthal symmetry needs to be broken, this can be achieved if the outer disc is not perfectly symmetric, which is most likely the case, or if the center of the two discs do not exactly coincide, or in the case of a warped stream entering the orbit, it also has a non axis-symmetric potential which can lead to mutual torques with the disc reducing the amplitude of the AM. We find that in some cases the torques can act to increase or not affect the AM of the accreting cold gas, leaving the cold gas with a high spin parameter, and thus the cold gas can't immediately join the disc, creating a more extended outer disc with time.

These points suggest a modification of the standard picture of the acquisition of AM by DM halos and consequently by disc galaxies. The new picture we suggest is presented in a simplified way using a cartoon in figure 5.1, and consists of four main stages separated to four regions:

1. **Linear tidal torques from the cosmic web:** As torques are the only means by which AM can be obtained, the first stage is essentially the same as linear TTT in the context of the cosmic web filaments. Filaments can acquire side way motion by the surrounding mass distribution or neighboring filaments, and thus acquire some impact parameter relative to the node they are attracted to. These torques act on all

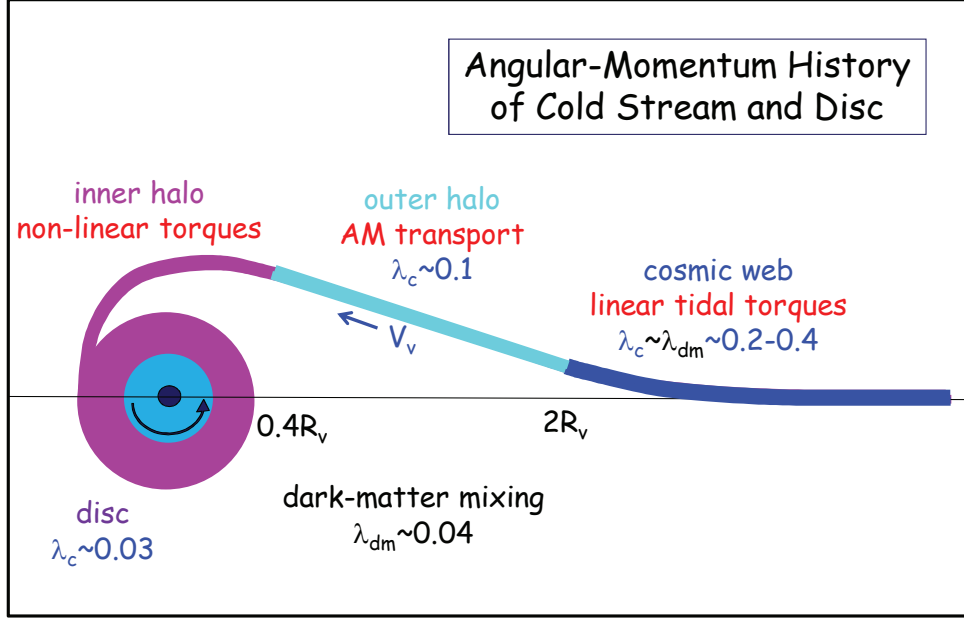


Figure 5.1: Origin of Angular Momentum in galaxies in four steps: from the cosmic web tidal torques, transport through the dark halo, exchange in the disc vicinity, redistribution within the disc due to outflows and violent disc instability (VDI).

the components leading to comparable spin parameters at large radii at early times. This takes place at $> 2R_v$.

2. **AM transport to the halo:** The AM is then transported either along the filaments for the cold dense gas and part of the DM or in a more isotropic way for the other components. In this accretion process, the AM is not altered much, as torques are weak in this region. However, within the halo the spin parameter of the different components can change significantly. This change is due to mixing of the AM of the different particles. The DM, baryons and hot gas components get mixed with material accreted previously with smaller specific AM and possibly with AM in different orientations leading to significant vector cancellation resulting in smaller specific AM. This is particularly significant for the DM component which virializes within the halo and cannot cool and collapse to the center as the baryons, but has orbits going all the way to the outer halo. On the other hand, the coherent, unperturbed accretion of the cold gas and the short time to reach the disc region results in less mixing and

a more coherent addition of the individual AM vectors leading to a higher specific AM. Despite that, the different streams can have different orientations relative to the disc which results in the reduction of the spin parameter from ~ 0.3 to ~ 0.1 , however the cold gas is still more coherent than the other components and thus still dominates the specific AM also within the halo.

3. **Non-linear torques in the 'Messy Region':** The cold filamentary gas which falls in the halo on a ballistic trajectory with an impact parameter $< 0.3R_v$ is halted by its AM when it reaches this distance from the disc center, it dissipates some of its velocity which allows it to enter into an orbit around the disc region. By this it defines the limit of this region by adding to it more cold dense gas with higher impact parameter, forming an extended outer disc, tilted with respect to the inner disc. Once in this region the cold gas experiences torques causing it to lose some AM, move to smaller radii in less than an orbital period, and become increasingly aligned with the disc spin axis, finally the gas reaches the disc and extends it in an inside-out fashion.
4. **Processes within the disc:** Once in the disc, outflows from stellar feedback and violent disc instability can preferentially remove low AM from the disc and transport AM from the inside out.

5.2 Open questions and caveats

- **The Cosmic Web:** What is the origin of the planarity of the streams and the typical number of streams? Can it be traced to the properties of the Gaussian random field? What determines the dominant stream, and the relative orientation of the different streams? How exactly do the streams acquire their AM in the form of an impact parameter?
- **AM and torques:** What is the nature of the torques? Is the disc the source of the torques? Does dynamical friction play a role for example on the clumps in the streams? What happens to the gas with negative AM? Does it get reoriented by the torques, or mixed with positive AM material? How do strong outflows change this picture of the messy region? Similarly, How does higher resolution change this picture? Does it increase the importance of the pressure torques?
- The analysis of the cold streams and the conclusions regarding the cosmic web, were done using only the gas, and not the DM, it is therefore possible that there be some differences when considering the DM cosmic web, although we believe the behavior should be similar as argued already.
- The distinction of cold and hot gas using a single temperature limit at all times, may contaminate the hot gas with gas that was not shock heated, thus increasing the hot gas specific AM.

- The AM calculation is highly sensitive to the choice of the rest frame. We tested some of the results with different rest frames, other than the galaxy center and rest frame, and found that although the qualitative results remain, the numerical values can change by 10s of percents.
- The torques calculation is also very sensitive to the correct choice of the center of the galaxy, especially for the gravitational torques.
- We have seen that satellites can heavily contaminate the torque results. Despite their familiar signature, it is not clear how much they affected the results in the inner region.

5.3 Suggested observations and future work

The notion of cold accretion through filaments is not yet well established observationally despite the clear evidence from theory and simulations. This has to do with a number of reasons including, low covering fractions (~ 3 thin filaments), low density compared to the inter stellar medium and signal swamped by outflows. The main probe for detection of cold gas is in absorption of neutral Hydrogen (HI) specifically the Lyman- α line, as the cold gas is expected to have low metallicity. Our result on the messy region being directly related to the cold mode accretion through cold streams and showing mainly rotational motion, has clear observational signal in the form of shifted absorption line (either blue or redshifted). This can be achieved in a setup consisting of a background quasar and a foreground galaxy, such that the two are separated along the line of sight. In such a way, by looking at different separations from the galaxy, at a given radius one should find increased shift in the absorption line towards higher velocities ranging between 0 and the disc rotation velocity, as a function of the separation from the galaxy towards the center. The outer extended disc, can be tilted with respect to the disc plane, therefore one should look also outside the inner disc plane. Another possible observational signature of the results regarding the AM of the streams, is the presence of counter rotating stellar disc, at a different radii and possibly different ages compared to the co-rotating disc. This can serve as evidence for accretion from two opposing cold streams through the messy region, accreting into the disc at different times. The future work consists of focusing on two regions, one is the region of the extended cosmic web which we did not fully address, this includes going further than $2R_v$, and examine the processes in which the streams acquire their AM through the impact parameter. this can involve the calculation of the inertia tensor and the tidal field in the region of individual filaments. The second region is the messy region, in which the use of tracer particles can allow to trace the exact motion of a given cold stream and follow its path to the disc. Finally, focus on the disc more closely, and examine the AM distribution within it and the effect of outflows on the disc AM by measuring the AM of the blown material, as well as the effect of VDI on the AM distribution within the disc.

Bibliography

- Adelman-McCarthy, J. K. (2008). The Sixth Data Release of the Sloan Digital Sky Survey. *ApJS*, 175:297.
- Algorry, D. G., Navarro, J. F., Abadi, M. G., Sales, L. V., Steinmetz, M., and Piontek, F. (2013). Counterrotating Stars in Simulated Galaxy Disks. *ArXiv e-prints*.
- Aragon-Calvo, M. A., van de Weygaert, R., and Jones, B. J. T. (2010). Multiscale phenomenology of the cosmic web. *MNRAS*, 408:2163–2187.
- Bardeen, M. J., Bond, R. J., Kaiser, N., and Szalay, S. A. (1986). The statistics of peaks of Gaussian random fields. *ApJ*, 304:15–61.
- Binney, J. and Tremaine, S. (2008). *Galactic Dynamics (second edition)*. Princeton University Press.
- Birnboim, Y. and Dekel, A. (2003). Virial shocks in galactic haloes? *MNRAS*, 345:349–364.
- Bond, J. R., Kofman, L., and Pogosyan, D. (1996). How filaments of galaxies are woven into the cosmic web. *Nature*, 380:603–606.
- Bouche, N., Murphy, M. T., Kacprzak, G. G., Peroux, C., Contini, T., Martin, C. L., and Dessauges-Zavadsky, M. (2013). Signatures of Cool Gas Fueling a Star-Forming Galaxy at Redshift 2.3. *Science*, 341:50–53.
- Brooks, A. M., Governato, F., Quinn, T., Brook, C. B., and Wadsley, J. (2009). THE ROLE OF COLD FLOWS IN THE ASSEMBLY OF GALAXY DISKS. *ApJ*, 694:396.
- Bullock, J. S., Dekel, A., Kolatt, T. S., Kravtsov, A. V., Klypin, A. A., Porciani, C., and Primack, J. R. (2001). A Universal Angular Momentum Profile for Galactic Halos. *ApJ*, 555:240–257.
- Ceverino, D., Dekel, A., Mandelker, N., Bournaud, F., Burkert, A., Genzel, R., and Primack, J. (2012). *MNRAS*, 420:3490–3520.
- Colless, M. (1999). First results from the 2dF Galaxy Redshift Survey. *Phil. Trans. R. Soc. Lond. A*, 357:105–116.

- Danovich, M., Dekel, A., Hahn, O., and Teyssier, R. (2012). Coplanar streams, pancakes and angular-momentum exchange in high- z disc galaxies. *MNRAS*, 422:1732–1749.
- Dekel, A. (1981). Imprints of the damping of adiabatic perturbations. *A&A*, 101:79–+.
- Dekel, A., Birnboim, Y., Engel, G., Freundlich, J., Goerdt, T., Mumcuoglu, M., Neistein, E., Pichon, C., Teyssier, R., and Zinger, E. (2009). Cold streams in early massive hot haloes as the main mode of galaxy formation. *Nature*, 457:451–454.
- Doroshkevich, A. G. (1970). Spatial structure of perturbations and origin of galactic rotation in fluctuation theory. *Astrophysics*, 6:320.
- Dutton, A. A. and van den Bosch, C. F. (2012). The angular momentum of disc galaxies: implications for gas accretion, outflows, and dynamical friction. *MNRAS*, 421:608–620.
- Fall, S. M. and Efstathiou, G. (1980). Formation and rotation of disc galaxies with haloes. *MNRAS*, 193:189–206.
- Hahn, O., Porciani, C., Marcella Carollo, C., and Dekel, A. (2007). Properties of Dark Matter Haloes in Clusters, Filaments, Sheets and Voids. *MNRAS*, 375:489–499.
- Hucra, J., Latham, D., and Tonry, J. (1983). The CfA redshift survey. *ApJS*, 52:89.
- Kimm, T., Devriendt, J., Slyz, A., Pichon, C., Kassin, S. A., and Dubois, Y. (2011). The angular momentum of baryons and dark matter halos revisited. *arXiv:1106.0538*.
- Klypin, A., Trujillo-Gomez, S., and Primack, J. (2011). Halos and galaxies in the standard cosmological model: results from the Bolshoi simulation. *arXiv:1002.3660v4*.
- Klypin, A. A. and Shandarin, F. S. (1983). Three-dimensional numerical model of the formation of large-scale structure in the Universe. *MNRAS*, 204:891–907.
- Kravtsov, A. V., Klypin, A. A., and Khokhlov, A. M. (1997). *ApJS*, 117:73.
- Mo, H. J., Mao, S., and White, S. D. M. (1998). The formation of galactic discs. *MNRAS*, 295:319–336.
- Padmanabhan, T. (2008). *Theoretical Astrophysics. Volume III: Galaxies and Cosmology*. Cambridge University Press.
- Peebles, P. J. E. (1969). Origin of the Angular Momentum of Galaxies. *ApJ*, 155:393.
- Pichon, C., Pogosyan, D., Kimm, T., Slyz, A., Devriendt, J., and Dubois, Y. (2011). Rigging dark haloes: why is hierarchical galaxy formation consistent with the inside-out build-up of thin discs? *MNRAS*, 418:2493–2507.
- Rees, M. J. and Ostriker, J. P. (1977). Cooling, dynamics and fragmentation of massive gas clouds - Clues to the masses and radii of galaxies and clusters. *MNRAS*, 179:541–559.

- Shen, J., Abel, T., and Sheth, R. K. (2006). An Excursion Set Model of the Cosmic Web: The Abundance of Sheets, Filaments, and Halos. *ApJ*, 645:783.
- Springel, V., White, S. D. M., Jenkins, A., and Frenk, C. S. (1996). Simulations of the formation, evolution and clustering of galaxies and quasars. *Nature*, 435:603–606.
- Steinmetz, M. and Bartelmann, M. (1984). On the spin parameter of dark-matter haloes. *ApJ*, 286:38–41.
- Stewart, K. R., Brooks, B. M., Bullock, J. S., Maller, A. H., Diemand, J., Wadsley, J., and Leonidas, M. A. (2013). Angular momentum aquisition in galaxy halos. *ApJ*, 74:769.
- Tillson, H., Devriendt, D., Slyz, A., Miller, L., and Pichon, C. (2012). Angular momentum transfer to a Milky Way disk at high redshift. *arXiv:1211.3124*.
- White, S. D. M. (1984). Angular momentum growth in protogalaxies. *ApJ*, 286:38–41.
- Zeldovich, Y. B. (1970). Gravitational instability: an approximate theory for large density perturbations. *A&A*, 5:84–89.